

REPORT DOCUMENTATION PAGE

Form Approved
OMB No. 0704-0188

The public reporting burden for this collection of information is estimated to average 1 hour per response, including the time for reviewing instructions, searching existing data sources, gathering and maintaining the data needed, and completing and reviewing the collection of information. Send comments regarding this burden estimate or any other aspect of this collection of information, including suggestions for reducing the burden, to Department of Defense, Washington Headquarters Services, Directorate for Information Operations and Reports (0704-0188), 1215 Jefferson Davis Highway, Suite 1204, Arlington, VA 22202-4302. Respondents should be aware that notwithstanding any other provision of law, no person shall be subject to any penalty for failing to comply with a collection of information if it does not display a currently valid OMB control number.

PLEASE DO NOT RETURN YOUR FORM TO THE ABOVE ADDRESS.

1. REPORT DATE (DD-MM-YYYY)	2. REPORT TYPE	3. DATES COVERED (From - To)
	Final Performance	5/01/04 - 4/30/07
4. TITLE AND SUBTITLE		5a. CONTRACT NUMBER
Investigation into the Combined Effects of Compaction, Strain Rate and Anisotropic Damage of a Geologic Target on the Trajectory Stability of Rigid Penetrators		5b. GRANT NUMBER FA9550-04-1-0156
		5c. PROGRAM ELEMENT NUMBER
		5d. PROJECT NUMBER
		5e. TASK NUMBER P00003
		5f. WORK UNIT NUMBER
6. AUTHOR(S) Dr. Oana Cazacu Dr. Ioan R. Ionescu <i>oleson</i> <i>Ioan R. Ionescu</i>		7. PERFORMING ORGANIZATION NAME(S) AND ADDRESS(ES) University of Florida College of Engineering 339 Weil Hall Gainesville, FL 32611
9. SPONSORING/MONITORING AGENCY NAME(S) AND ADDRESS(ES) AFAF, AFRL AF Office of Scientific Research 875 N. Randolph Street, Room 3112 Arlington, VA 22203 <i>Dr. Alan Nachman/ME</i>		8. PERFORMING ORGANIZATION REPORT NUMBER AFOSR/PKR3
		10. SPONSOR/MONITOR'S ACRONYM(S)
		11. SPONSOR/MONITOR'S REPORT NUMBER(S)
12. DISTRIBUTION/AVAILABILITY STATEMENT <i>Distribution Statement A: unlimited</i>		AFRL-SR-AR-TR-07-0347
13. SUPPLEMENTARY NOTES		

14. ABSTRACT

This report presents the results of an experimental investigation into the combined effects of inelasticity and strain rate sensitivity on penetration into geologic or geological derived targets. Both material models and specific computational methods have been developed. A new class of compressible rigid viscoplastic models were proposed to capture the solid-fluid transition in behavior at high strain rates, account for damage/plasticity couplings and viscoelastic effects which are observed in geological and cementitious materials. A hybrid time-discretization was used to model the non-stationary flow of the target material and the projectile-target interaction, i.e. an explicit Euler method for the projectile equation and a forward (implicit) method for the target boundary value problem. At each time step, a mixed finite-element and finite-volume strategy was used to solve the "target" boundary value problem. Specifically, the nonlinear variational inequality for the velocity field was discretized using the finite element method while finite volume method was used for the hyperbolic mass conservation and damage evolution equations.

15. SUBJECT TERMS

Penetration, Compressible Fluids, Concrete.

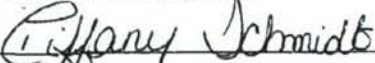
16. SECURITY CLASSIFICATION OF: a. REPORT b. ABSTRACT c. THIS PAGE			17. LIMITATION OF ABSTRACT	18. NUMBER OF PAGES	19a. NAME OF RESPONSIBLE PERSON <i>Roslyn S. Oleson</i>
					19b. TELEPHONE NUMBER (Include area code) (352) 392-9447 x 7

Standard Form 298 (Rev. 8/98)

Prescribed by ANSI Std. Z39-18

ROSLYN S. OLESON
ASSISTANT DIRECTOR OF RESEARCH
UNIVERSITY OF FLORIDA

SF 269
Project 00048814
Dept. ID 19120100

FINANCIAL STATUS REPORT (Short Form)				PAC 00040448 4/30/07	
1. Federal Agency and Organizational Element to which Report is Submitted US Air Force	2. Federal Grant Number or Other Identifying Number Assigned by Federal Agency FA9550-04-1-0156	OMB APPROVAL No. 0348-0038	Report No. #1 FINAL		
3. Recipient Organization (Name and complete address, including ZIP code) Engineering and Industrial Experiment Station University of Florida 340 Weil Hall P.O. Box 116550 Gainesville, FL 32611-6550					
4. Employer Identification Number 596002052	5. Recipient Account Number or Identifying Number 00048816/00062562	6. Final Report XX YES NO	7. Basis <input type="checkbox"/> CASH <input checked="" type="checkbox"/> ACCRUAL		
8. Funding/Grant Period From: (Month, Day, Year) 05/01/2004	To: (Month, Day, Year) 04/30/2007	9. Period Covered by this Report From: (Month, Day, Year) 05/01/04	To: (Month, Day, Year) 04/30/07		
10. Transactions:		I Previously Reported	II This Period	III Cumulative	
a. Total outlays		\$0.00	\$111,906.21	\$111,906.21	
b. Recipient share of outlays		0.00	0.00	\$0.00	
c. Federal share of outlays		\$0.00	\$111,906.21	\$111,906.21	
d. Total unliquidated obligations				0.00	
e. Recipient share of unliquidated obligations				0.00	
f. Federal share of unliquidated obligations				0.00	
g. Total Federal share (Sum of lines c and f)				111,906.21	
h. Total Federal funds authorized for this funding period				111,917.00	
i. Unobligated balance of Federal funds (Line h minus line g)				\$10.79	
11. Indirect Expense	a. Type of Rate (Place "X" in appropriate box) <input type="checkbox"/> Provisional <input checked="" type="checkbox"/> Predetermined <input type="checkbox"/> Final <input type="checkbox"/> Fixed				
	b. Rate 25.0% 45.5%	c. Period 05/01/04-04/30/07 05/01/06-04/30/07	d. Base \$65,929.74 \$20,271.00	d. Total Amount \$16,482.47 \$9,223.00	e. Federal Share \$25,705.47
12. Remarks: Attach any explanation deemed necessary or information required by Federal sponsoring agency in compliance with governing legislation					
TOTAL DIRECT 05/01/04-04/30/07 05/01/06-04/30/07		TUITION \$65,929.74 \$20,271.00	Equipment \$0.00 \$0.00	= BASE \$65,929.74 \$20,271.00	
13. Certification: I certify to the best of my knowledge and belief that this report is correct and complete and that all outlays and unliquidated obligations are for the purposes set forth in the award documents.					
Typed or Printed Name and Title Tiffany Schmidt, Assistant Director			Telephone (Area code, number, and extension) (352) 392-6626 FAX: (352) 392-7063		
Signature of Authorized Certifying Official 			Date Report Submitted 7/11/07		

FINAL REPORT GRANT F-9550-04-1-0156

Investigation into the combined effects of compaction, strain rate sensitivity, and anisotropic damage of a geologic target on the trajectory stability of rigid penetrators.

Award: 5/1/2005

Program Manager: Dr. Arje Nachman

Oana Cazacu¹ and Ioan R. Ionescu²

¹ Department of Mechanical and Aerospace Engineering, University of Florida
Graduate Engineering & Research Center,
1350 N. Poquito Rd Shalimar, FL 32579,
E-mail: cazacu@reef.ufl.edu

² Laboratoire de Mathématiques, Université de Savoie,
Campus Scientifique, 73376 Le Bourget-du-Lac Cedex, France
E-mail: ionescu@univ-savoie.fr

20070920023

Contents

1	SUMMARY	3
2	Task 1: Development of a new class of fluid-like constitutive models for porous materials	4
2.1	Introduction	4
2.2	Rigid viscoplastic fluids	5
2.3	Perzyna-type fluids	8
2.3.1	Mises fluid	10
2.3.2	Mises fluid, revisited	11
2.3.3	Modified Cam-Clay fluid of Perzyna's type	14
2.4	Superposition method	15
2.4.1	Bingham Fluid	17
2.4.2	Bingham fluid, revisited	18
2.4.3	Superposed Cam-Clay fluid	19
2.4.4	CAP fluid	20
2.5	It does not always work	21
2.6	Examples of the models' response	23
2.6.1	Bingham fluid, revisited	24
2.6.2	Cam-clay fluid	27
2.7	On the choice of internal parameters	27
2.8	Conclusions	29
3	Task 2: Numerical modeling of projectile penetration into compressible rigid visco-plastic media	33
3.1	Introduction	33
3.2	Constitutive model for the target material	35
3.3	Geometry and fields equations	37
3.4	The algorithm	40
3.4.1	Time discretization	40
3.4.2	The general scheme	41
3.4.3	The velocity problem	41
3.4.4	The density/damage problem	44
3.5	Numerical results	45
3.5.1	Geometrical and physical settings	45
3.5.2	Time step sensitivity	47
3.5.3	Fields distribution in the target	48
3.5.4	Parameter sensitivity of the penetration depth	50
4	Conclusions	53

1 SUMMARY

This report presents the results of an experimental investigation into the combined effects of inelasticity and strain rate sensitivity on penetration into geologic or geological derived targets. Both material models and specific computational methods have been developed. A new class of compressible rigid viscoplastic models were proposed to capture the solid-fluid transition in behavior at high strain rates, account for damage/plasticity couplings and viscous effects which are observed in geological and cementitious materials.

A hybrid time-discretization was used to model the non-stationary flow of the target material and the projectile-target interaction, i.e. an explicit Euler method for the projectile equation and a forward (implicit) method for the target boundary value problem. At each time step, a mixed finite-element and finite-volume strategy was used to solve the "target" boundary value problem. Specifically, the nonlinear variational inequality for the velocity field was discretized using the finite element method while a finite volume method was used for the hyperbolic mass conservation and damage evolution equations. To solve the velocity problem, a decomposition-coordination formulation coupled with the augmented lagrangian method was adopted.

Numerical simulations of penetration into concrete were performed. By conducting a time step sensitivity study it was shown that the numerical model is robust and computationally inexpensive. For the constants involved in the model (shear and volumetric viscosities, cut-off yield limit and exponential weakening parameter for friction) that cannot be determined from data, a parametric study was performed. It is shown that using the material model and numerical algorithms developed the evolution of the density changes around the penetration tunnel, the shape and location of the rigid/plastic boundary, of the compaction zones and of the extent of damage due to air void collapse are described accurately.

2 Task 1: Development of a new class of fluid-like constitutive models for porous materials

2.1 Introduction

A general framework for modeling the non-linear behavior of cementitious or geological materials for applications involving dynamic loading is offered by viscoplasticity theory. In the elastic/viscoplastic models with non-stationary yield surface the central idea is that the loading function depends on the stress state, the plastic history of the material through the plastic strains, and a scalar parameter which embodies time dependent alteration of the material properties. A very large number of models developed for inviscid behavior have been extended into the rate-dependent range using the overstress concept. However, most of these models have been developed in support of civil engineering applications and thus are in general representative of relatively small strains and low strain rate behavior.

In some processes, such as impact or high velocity penetration into cementitious or geological materials, large deformations, high pressures and high strain rates occur. That is why in the mechanical and numerical modeling, an Eulerian description and a fluid-type constitutive law seems to be more suitable. Fluid-type constitutive equations have been used to describe the high-strain rate behavior of metallic materials (see for instance Batra, 1987; Batra and Li, 1988). Implicit in these models is the hypothesis of incompressibility, hence those models cannot describe the observed irreversible volumetric changes observed in geological and cementitious materials. To account for the effect of compaction on the response of cementitious or geological materials, an explicit dependence of both the yield limit and the viscosity coefficients on the current density has to be considered (e.g. Cazacu et al., 2004).

It is well recognized that depending on their dynamical state, particulate materials may display both solid and fluid like behavior. Since at low deformation rates the behavior is mainly dictated by frictional interparticle contact and sliding of the particles over each other, a large body of literature exists in which particulate systems are modeled using a solid mechanics approach. These models are generally developed within the framework of plasticity theory. Again, in order to model short-term time effects on the quasi-static deformation of such systems, extensions of the inviscid models using Perzyna's approach (Perzyna, 1966) have been proposed. However, most of these models are applicable only for relatively small strains and low strain rates. On the other hand, rapid unfluidized flows such as chute flows and avalanches in which particles interact by short collisions and cascade over each other, are generally modeled based on analogy to gas dynamics (e.g. Jenkins and Askari, 1991; Campbell and Brennen, 1985).

Non-linear viscous compressible equations have been also used for prediction of chute flows as well as for describing slowly-moving natural slopes which generally have a displacement history of few millimeters per year followed by periods of acceleration degenerating into catastrophic events (e.g. Vulliet, 2000). A combination

of the two approaches was also proposed (e.g. Savage, 1979; Goodman and Cowin (1971). For example, the premise of the model proposed by Goodman and Cowin (1971) is that at rest the granular material obeys a Coulomb yield condition. Once the flow develops the state of stress is a function of the rate of deformation and the change in volume distribution, with the dissipative part of the stress (i.e. the part of stress that depends on the deformation rate) being that of a viscous fluid. Starting from the non-linear viscous model of Savage(1979), recently Elaskar and Godoy (1998) have proposed a non-linear compressible viscous model of granular flow with second-order effects.

Experimental evidence indicates that for a wide range of porous and particulate materials flow develops only if a certain threshold that depends on the stress level and the density or the solids volume fraction is exceeded. At difference with a classical fluid model, in the absence of motion such materials can sustain a shear stress. Generally, in order to describe the behavior of such materials, it is necessary to formulate a flow activation condition or yield condition that describes the state of stress in the material at the onset of the deformation process and to describe the state of stress in the material, once the flow/deformation develops. Moreover, the elastic effects can be neglected, hypothesis which is usually made when describing the large deformation behavior of particulate materials or cementitious materials.

The main objective of this work is to provide procedures for constructing compressible viscoplastic fluid-type constitutive models compatible with a given flow initiation criterion. Two methods will be considered: Perzyna's viscoplastic regularization, and a Maxwell type stress superposition method. Examples of constitutive equations obtained from classical yield functions using both procedures are presented. Illustrations of the response of these models for uniaxial compression conditions as well as comparisons between these various models are provided. Furthermore, we show that irrespective of the method used, for certain yield conditions the resulting mechanical model is physically unacceptable. That means that not from all yield conditions can a fluid-type model be deduced. Extensions of these models that include coupling between damage, plastic and viscous effects are proposed. Some results of numerical modeling of penetration into concrete using a compressible rigid-viscoplastic model are presented. Finally, extensions of fluid-type models that include coupling between damage, plastic and viscous effects are proposed.

2.2 Rigid viscoplastic fluids

Let us begin by describing what we mean by a rigid viscoplastic fluid. In contrast with a classical fluid, which cannot sustain a shear stress, we suppose that at rest the Cauchy stress tensor σ must belong to an admissible convex set K of $\mathbb{R}_S^{3 \times 3}$, the space of second order symmetric tensors over the set of real numbers \mathbb{R} . Conversely, if the stress is in K then the rate of deformation tensor $D = D(\mathbf{v}) = (\nabla \mathbf{v} + \nabla^T \mathbf{v})/2$ (\mathbf{v} denotes the eulerian velocity field) vanishes. If the stress tensor is not in K then

there is flow, the rate of deformation tensor \mathbf{D} being subject to certain kinematic constraints, i.e. $\mathbf{D} \in \mathcal{C}$, and the stress tensor is a function of \mathbf{D}

$$\mathbf{D}(\mathbf{v}) \in \mathcal{C}, \quad \begin{cases} \boldsymbol{\sigma} = \mathbf{f}(\mathbf{D}(\mathbf{v})) & \text{if } |\mathbf{D}(\mathbf{v})| \neq 0, \\ \boldsymbol{\sigma} \in K & \text{if } |\mathbf{D}(\mathbf{v})| = 0, \end{cases} \quad (1)$$

It should be noted that at difference with a classical fluid constitutive equation, for a rigid viscoplastic material the function \mathbf{f} is not defined and cannot be prolonged by continuity in $\mathbf{D} = 0$. To ensure continuous transition between flow and no-flow states, it is necessary to impose that only the limit points of $\mathbf{f}(\mathbf{D})$ when $\mathbf{D} \rightarrow 0$ are in K , i.e.

$$\text{if } \mathbf{D} \rightarrow 0 \text{ with } \mathbf{D} \in \mathcal{C} \text{ and } \mathbf{f}(\mathbf{D}) \rightarrow \boldsymbol{\sigma} \text{ then } \boldsymbol{\sigma} \in K. \quad (2)$$

The condition (2) implies that we neglect the elastic properties of the material. Such a hypothesis is valid in the high pressure regime in which elastic strains are much smaller than inelastic strains. Also, what we usually call the "static pressure" (i.e. the pressure that the material may sustain for zero volume deformation rate) is not directly present in the model. In order to capture the effect of the porosity on the behavior of geological materials (e.g. pore closure, pore collapse), the convex set K and \mathbf{f} are considered to be functions of h , an internal state variable related to the actual irreversible volume change. Since elastic effects are neglected, $dh = \text{div}(\mathbf{v})dt$ and based on the continuity equation

$$\frac{d\rho}{dt} = \frac{\partial \rho}{\partial t} + \mathbf{v} \cdot \nabla \rho = -\rho \text{div}(\mathbf{v}) \quad (3)$$

where ρ is the actual density, it follows that $d\ln(\rho) = dh$. Thus, the actual density can be considered as internal variable (see the last section for other choices of the internal state variable h). In the following, the convex $K = K(\rho)$ will be defined through a continuous scalar function $F = F(\boldsymbol{\sigma}, \rho)$ that describes the flow/no flow condition, i.e.

$$K(\rho) = \{\boldsymbol{\sigma} \in \mathbb{R}_S^{3 \times 3} ; F(\boldsymbol{\sigma}, \rho) \leq 0\}.$$

From classic representation theorems for isotropic tensor functions, it follows that there exist three scalar functions α, β, γ which depend on \mathbf{D} through its three invariants such that

$$\mathbf{f}(\mathbf{D}, \rho) = \alpha(\mathbf{D}, \rho)\mathbf{I} + \beta(\mathbf{D}, \rho)\mathbf{D}' + \gamma(\mathbf{D}, \rho)\mathbf{D}^2,$$

where \mathbf{I} is the second-order identity tensor, while \mathbf{A}' denotes the deviator of any symmetric second-order tensor \mathbf{A} , i.e. $\mathbf{A}' = \mathbf{A} - \text{tr}(\mathbf{A})/3\mathbf{I}$, and ' tr ' stands for the trace operator.

In the following, we will neglect second order effects, i.e. impose $\gamma = 0$ and consider that the constitutive functions do not depend on the third invariant of the

rate of deformation tensor. Henceforth, our discussion will be limited to a subclass of viscoplastic fluids characterized by:

$$\mathbf{D}(\mathbf{v}) \in \mathcal{C}, \quad \begin{cases} \boldsymbol{\sigma} = \alpha(\mathbf{D}(\mathbf{v}), \rho) \mathbf{I} + \beta(\mathbf{D}(\mathbf{v}), \rho) \mathbf{D}'(\mathbf{v}) & \text{if } |\mathbf{D}(\mathbf{v})| \neq 0, \\ F(\boldsymbol{\sigma}, \rho) \leq 0 & \text{if } |\mathbf{D}(\mathbf{v})| = 0, \end{cases} \quad (4)$$

where $\mathcal{C} \subset \mathbb{R}_S^{3 \times 3}$ represents a kinematic constraint.

The above constitutive equation completely describes a rigid viscoplastic fluid through only four elements : a (scalar) yield function F , a set \mathcal{C} of admissible strain rates and two scalar functions α and β . As expected, these four elements are not independent. In order to define a consistent rigid viscoplastic model compatibility conditions ought to be imposed.

The first two compatibility conditions concern the flow regime. Thus, if there is flow the associated stress $\boldsymbol{\sigma}$ has to be outside the convex K defined through the yield function F . In this case (i.e. in the viscoplastic regime where $\mathbf{D} \neq 0$) we have to impose that

$$F(\alpha(\mathbf{D}, \rho) \mathbf{I} + \beta(\mathbf{D}, \rho) \mathbf{D}', \rho) > 0, \quad \text{for all } \mathbf{D} \in \mathcal{C} \setminus 0. \quad (5)$$

This assumption is natural since the elastic effects are neglected (i.e. a rigid subdomain is included in the constitutive domain).

The second compatibility condition seems also to be natural. Since we model a fluid-type behavior, we suppose that $\boldsymbol{\sigma}$ is continuous with respect to \mathbf{D} , i.e.

$$\mathbf{D} \rightarrow \alpha(\mathbf{D}, \rho), \quad \mathbf{D} \rightarrow \beta(\mathbf{D}, \rho) \text{ are continuous on } \mathcal{C} \setminus 0. \quad (6)$$

That means that small variations in the rate of deformation $\mathbf{D} \neq 0$ will give small variations in the stress field. Let us stress again that for a rigid-viscoplastic fluid this property is not valid in the neighborhood of $\mathbf{D} = 0$.

The third condition deals with the "continuity" of the transition between flow and no flow. More precisely, the stress associated to a fluid in motion which tends to stop flowing has to approach the yield surface (i.e. the boundary of K). For the particular form of the constitutive equation (65), the condition (2) becomes

$$F(\alpha(\mathbf{D}, \rho) \mathbf{I} + \beta(\mathbf{D}, \rho) \mathbf{D}', \rho) \rightarrow 0, \quad \text{for } \mathbf{D} \rightarrow 0 \text{ with } \mathbf{D} \in \mathcal{C} \setminus 0. \quad (7)$$

The fourth and last compatibility condition yields from thermodynamic arguments. It states that the dissipated power during viscoplastic flow is positive $\boldsymbol{\sigma} : \mathbf{D} \geq 0$, i.e.

$$\alpha(\mathbf{D}, \rho) \text{tr}(\mathbf{D}) + \beta(\mathbf{D}, \rho) |\mathbf{D}'|^2 \geq 0 \quad \text{for all } \mathbf{D}. \quad (8)$$

Our main goal is to provide procedures for determining the expressions of the constitutive functions F , α , and β such that the model (65) is consistent (i.e. the compatibility conditions (5-8) are satisfied). Specifically, we will use two methods.

The first one is Perzyna's visco- plastic regularization approach while the second one is based on a Maxwell type superposition of a rigid plastic material on a compressible viscous fluid. We illustrate the proposed approach by providing examples of constitutive equations obtained starting from classic yield functions by making use of both procedures. In general, even if we start from the same yield condition, the models obtained using these two methods are different.

Furthermore, we show that starting from certain classical yield functions, we can construct consistent fluid-type models, while for other classical yield functions, irrespective of the procedure followed, the constitutive functions α and β cannot be determined or the resulting kinematic constraints are physically unacceptable.

We shall suppose in the following that α, β depend on \mathbf{D} through its two first invariants

$$d = \text{tr}(\mathbf{D}), \quad e = |\mathbf{D}'|, \quad (9)$$

i.e. $\alpha = \alpha(d, e, \rho), \beta = \beta(d, e, \rho)$, while the flow-no flow function $F(\boldsymbol{\sigma}, \rho)$ depends on $\boldsymbol{\sigma}$ through the invariants

$$p = \frac{\text{tr}(\boldsymbol{\sigma})}{3}, \quad q = \sqrt{\frac{3}{2}} |\boldsymbol{\sigma}'|, \quad (10)$$

i.e. $F = F(p, q, \rho)$. From (65) follows that for $\mathbf{D} \neq 0$:

$$q = \sqrt{\frac{3}{2}} \beta(d, e, \rho) e, \quad p = \alpha(d, e, \rho). \quad (11)$$

2.3 Perzyna-type fluids

A general procedure for extending any inviscid elastic/ plastic model such as to account for rate effects was proposed by Perzyna. According to Perzyna's theory (1966), viscous plastic flow follows a time-dependent flow rule and occurs only if the stress exceeds the yield limit.

Let ϕ be a scalar function such that $\phi(x) = 0$ for $x \leq 0$ while for $x > 0$, we have $\phi(x) > 0$ and ϕ is monotonically increasing. Denoting by $\eta > 0$ the viscosity coefficient, we consider the following representation of the rate of deformation

$$\mathbf{D} = \frac{1}{2\eta(\rho)} \phi(F(\boldsymbol{\sigma}, \rho)) [A(\boldsymbol{\sigma}, \rho)I + B(\boldsymbol{\sigma}, \rho)\boldsymbol{\sigma}' + C(\boldsymbol{\sigma}, \rho)\boldsymbol{\sigma}^2], \quad (12)$$

where F is the yield function and A, B and C are scalar functions which depend on the stress invariants and on the density ρ which plays the role of hardening parameter (see last section for a discussion concerning other choices for the internal variables).

An important class of materials can be derived by assuming the existence of a viscoplastic potential, i.e. the existence of a function $G(\boldsymbol{\sigma}, \rho)$ such that

$$A(\boldsymbol{\sigma}, \rho)I + B(\boldsymbol{\sigma}, \rho)\boldsymbol{\sigma}' + C(\boldsymbol{\sigma}, \rho)\boldsymbol{\sigma}^2 = \frac{\partial G(\boldsymbol{\sigma}, \rho)}{\partial \boldsymbol{\sigma}}. \quad (13)$$

Generally, it is also assumed that flow is associated, i.e. that G coincides with the yield function F . However, for granular or porous materials, the experimental evidence suggests that the hypothesis of flow normality does not apply, and the more general representation (12) of the rate of deformation ought to be used.

We seek to obtain a model of type (65) from (12), i.e. to deduce explicit expressions for the constitutive functions α and β as well as the kinematic restrictions resulting from enforcing the compatibility conditions (5) to (8). Hence, in (12) we neglect the influence of the third stress invariant and take $C = 0$ and further assume that the constitutive functions A and B as well as the viscosity coefficient η depend on the actual density, i.e.

$$\mathbf{D} = \frac{1}{2\eta(\rho)} \phi(F(p, q, \rho)) [A(p, q, \rho) \mathbf{I} + B(p, q, \rho) \boldsymbol{\sigma}']. \quad (14)$$

Using 15and(14), we obtain for $F(p, q, \rho) > 0$ the following nonlinear system in the unknowns p and q

$$\begin{cases} \frac{3}{2\eta(\rho)} \phi(F(p, q, \rho)) A(p, q) = d \\ \frac{1}{2\eta(\rho)} \sqrt{\frac{2}{3}} \phi(F(p, q, \rho)) q B(p, q) = e. \end{cases} \quad (15)$$

Let us denote by $\mathcal{S}_F(\cdot, \cdot, \rho) : \mathbb{R} \times \mathbb{R}_+ \rightarrow \mathbb{R} \times \mathbb{R}_+$, the function defined as $(e, d) = \mathcal{S}_F(p, q, \rho)$ through (15). Let $J_{\mathcal{S}_F}$ be the jacobian matrix of \mathcal{S}_F . Its determinant is equal to $3\sqrt{2/3}J/(16\eta(\rho)^2)$ with J given by

$$J = (\phi' A \partial_p F + \phi \partial_p A)(q \phi' B \partial_q F + q \phi \partial_q B + \phi B) - (\phi' A \partial_q F + \phi \partial_q A)(q \phi' B \partial_p F + q \phi \partial_p B) \quad (16)$$

For a particular choice of the constitutive functions A , B and F , the set of admissible rate of deformation \mathbf{D} is given by the image of the operator \mathcal{S}_F , i.e.

$$\mathcal{C} = \{\mathbf{D} \in \mathbb{R}_S^{3 \times 3}; \exists (p, q) \text{ with } F(p, q, \rho) \geq 0, \text{ such that } (d, e) = \mathcal{S}_F(p, q, \rho)\}, \quad (17)$$

while the invertibility of \mathcal{S}_F depends on the rank of $J_{\mathcal{S}_F}$ (given by J) and $\dim(\mathcal{C})$.

If \mathcal{S}_F is invertible, i.e. for all $(d, e) \in \mathcal{C}$ we can solve the system (15) and there exist P and Q such that

$$\begin{cases} p = P(d, e, \rho) \\ q = Q(d, e, \rho), \end{cases} \quad (18)$$

then

$$\alpha(d, e, \rho) = P(d, e, \rho), \quad \beta(d, e, \rho) = \sqrt{\frac{2}{3}} \frac{Q(d, e, \rho)}{e}. \quad (19)$$

Next, these expressions for α and β are substituted in the compatibility restrictions (5)-(8).

If the compatibility conditions are not satisfied, it means that it is not possible to construct a fluid-type model (65) using the regularization method of Perzyna (i.e. from the model (14)).

It is to be noted that if the hypothesis of associated flow rule applies and $\phi(x) = ([x]_+/F_0)^n$, where $[x]_+ = (|x| + x)/2$ and F_0 and n are constants, i.e.

$$A(p, q, \rho) = \frac{F_0}{3} \frac{\partial F}{\partial p}(p, q, \rho), \quad B(p, q, \rho) = \frac{3F_0}{2q} \frac{\partial F}{\partial q}(p, q, \rho),$$

then (15) is:

$$d = \frac{F_0^2}{2\eta(\rho)} \frac{\partial H}{\partial p}(p, q, \rho), \quad e = \frac{3F_0^2}{4\eta(\rho)} \sqrt{\frac{2}{3}} \frac{\partial H}{\partial q}(p, q, \rho), \quad \text{for } F(p, q, \rho) \geq 0, \quad (20)$$

with $H(p, q, \rho) = (F(p, q, \rho)/F_0)^{n+1}/(n+1)$. In this case the jacobian (16) has a simple form

$$J(p, q, \rho) = 2F_0^4 \left[\frac{\partial^2 H}{\partial p^2}(p, q, \rho) \frac{\partial^2 H}{\partial q^2}(p, q, \rho) - \left(\frac{\partial^2 H}{\partial p \partial q}(p, q, \rho) \right)^2 \right], \quad \text{for } F(p, q, \rho) \geq 0. \quad (21)$$

It is worth noting that if F is affine in p and q (e.g. Mises or Drucker-Prager yield functions) then J is always vanishing and $\dim(\mathcal{C}) < 6$, i.e. the flow has to satisfy certain kinematic restrictions. However, the resulting kinematic constraints have a clear physical meaning only for certain yield conditions. In the next subsection, we show that in the case of the von Mises yield condition, the kinematic constraint that ought to be fulfilled is the incompressibility condition. The use of a Drucker-Prager yield condition would lead to kinematic restrictions that do not have physical meaning (see section 5 for a detailed discussion).

2.3.1 Mises fluid

Consider the Mises yield condition $F(p, q) = \sqrt{\frac{2}{3}}q - \kappa$, where κ is the flow stress of the material in simple tension or compression. For associated flow, the system (20) reduces to

$$\begin{cases} 0 = d \\ \frac{F_0}{2\eta(\rho)} \left[\left(\sqrt{\frac{2}{3}}q - \kappa \right) / F_0 \right]^n = e. \end{cases}$$

The jacobian J is zero (see (21)) and the image of the operator \mathcal{S}_F is:

$$\mathcal{C} = \{ \mathbf{D} \in \mathbb{R}_S^{3 \times 3} ; \text{trace}(\mathbf{D}) = 0 \}, \quad (22)$$

i.e. the flow ought to be isochoric. Since $\dim(\mathcal{C}) = 5$, from (20), we cannot determine α . In other words, p cannot be determined from a knowledge of the deformation because of the restriction of material incompressibility. From (20) follows that $q = Q(e, d) = \sqrt{\frac{3}{2}}[\kappa + F_0(2\eta(\rho)e/F_0)^{1/n}]$ and (65) becomes:

$$\operatorname{div}(\mathbf{v}) = 0, \quad \begin{cases} \boldsymbol{\sigma} = \alpha \mathbf{I} + \frac{\kappa + F_0(2\eta(\rho)|\mathbf{D}(\mathbf{v})|/F_0)^{1/n}}{|\mathbf{D}(\mathbf{v})|} \mathbf{D}(\mathbf{v}) & \text{if } |\mathbf{D}(\mathbf{v})| \neq 0, \\ |\boldsymbol{\sigma}'| \leq \kappa & \text{if } |\mathbf{D}(\mathbf{v})| = 0, \end{cases} \quad (23)$$

with α undetermined. Equation (23) can also be viewed as a constitutive equation for an incompressible viscous fluid with viscosity equal to $(\kappa + F_0(2\eta(\rho)|\mathbf{D}(\mathbf{v})|/F_0)^{1/n})/|\mathbf{D}(\mathbf{v})|$.

For $n = 1$ and κ constant, (23) reduces to the three-dimensional form of the incompressible Bingham model due to Hohenemser and Prager (see for example, Prager and Hodge (1968)):

$$\operatorname{div}(\mathbf{v}) = 0, \quad \begin{cases} \boldsymbol{\sigma} = \alpha \mathbf{I} + (2\eta(\rho) + \frac{\kappa}{|\mathbf{D}(\mathbf{v})|}) \mathbf{D}(\mathbf{v}) & \text{if } |\mathbf{D}(\mathbf{v})| \neq 0, \\ |\boldsymbol{\sigma}'| \leq \kappa & \text{if } |\mathbf{D}(\mathbf{v})| = 0, \end{cases} \quad (24)$$

The Bingham constitutive equation (24) with flow stress κ constant is the most commonly used was used extensively to model the rate and time effects on the deformation of metallic materials (e.g. Batra and Lin, 1987). Bingham model is also the most commonly used model to describe fluids with yield stress such as slurries (e.g. aluminum slurries) and waxy crude oils (see for example, Alexandrou et al., 2003; Vinay et al., 2005).

However, a realistic description of the behavior of geological materials cannot neglect the dependence of yielding and subsequent flow on density. To account for this influence, Cristescu et al (2002) have used for the description of slow motion of natural slopes a Bingham model (24) with yield limit dependent on density $\kappa = \kappa(\rho)$. The main limitation of such a model is that the deformation is isochoric, which is a direct consequence of the form of the yield condition adopted.

2.3.2 Mises fluid, revisited

Implicit in the models of type (23) is the assumption of incompressibility. Also, such models cannot account for changes in density during loading. However, experimental studies of the dynamic behavior of cementitious materials have indicated a strong dependence of yielding and subsequent flow on density (see for instance experimental data on cementitious materials reported in Malvern et al., 1990; Ross et al., 1996; Schmidt et al., 2001 as well as Hugoniot data reported by Osborn, 1981).

To describe the high-pressure and high strain rate behavior of such materials, we propose an extension of the Bingham model. We assume that yielding under

deviatoric conditions is of Von Mises type with yield limit κ depending on the current density, i.e. $\kappa = \kappa(\rho)$. For hydrostatic conditions, the response is described by a pressure-density relationship of the form: $p = p_c(\rho)$. The specific expression of the function $p_c(\rho)$ is obtained from quasi-static and dynamic laboratory data as well as Hugoniot data. Since during unloading the reversible decrease of volume is very small, it can be neglected and therefore the unloading process is rigid (the density acquired at the end of the loading process is preserved during unloading). Thus, in order to capture both the effects of compaction on shear flow and changes in density during hydrostatic loading, we consider a yield condition of the form:

$$F(p, q, \rho) = \sqrt{\left[\sqrt{\frac{2}{3}}q - \kappa(\rho)\right]_+^2 + [p + p_c(\rho)]_-^2}. \quad (25)$$

where $[x]_+ = (|x| + x)/2$, $[x]_- = (|x| - x)/2$. Next, the model is constructed using the procedure outlined in section 3.1. Indeed, the system (20) becomes

$$\begin{cases} -\frac{1}{2\eta(\rho)}(F(p, q, \rho)/F_0)^{n-1}[p + p_c(\rho)]_- = d \\ \frac{1}{2\eta(\rho)}(F(p, q, \rho)/F_0)^{n-1}\left[\sqrt{\frac{2}{3}}q - \kappa(\rho)\right]_+ = e. \end{cases}$$

Note that it can be inverted for $d \leq 0$ or

$$\mathcal{C} = \{D ; \text{trace}(D) \leq 0\}.$$

These kinematic restrictions express that the flow is compressible and the unloading is rigid. Furthermore,

$$p = P(d, e, \rho) = -p_c(\rho) + d \frac{F_0(2\eta(\rho)\sqrt{d^2 + e^2}/F_0)^{1/n}}{\sqrt{d^2 + e^2}} \quad \text{for } d < 0$$

$$q = Q(d, e, \rho) = \sqrt{\frac{3}{2}}\left[\kappa(\rho) + e \frac{F_0(2\eta(\rho)\sqrt{d^2 + e^2}/F_0)^{1/n}}{\sqrt{d^2 + e^2}}\right], \quad \text{for } e \neq 0.$$

Further substitution into (65) leads to the following constitutive equation of a compressible rigid-viscoplastic fluid:

$$\begin{cases} \boldsymbol{\sigma}' = \left[\frac{F_0(2\eta(\rho)\sqrt{\text{div}(\mathbf{v})^2 + |\mathbf{D}'|^2}/F_0)^{1/n}}{\sqrt{\text{div}(\mathbf{v})^2 + |\mathbf{D}'|^2}} + \frac{\kappa(\rho)}{|\mathbf{D}'|} \right] \mathbf{D}' & \text{if } |\mathbf{D}'| \neq 0, \\ |\boldsymbol{\sigma}'| \leq \kappa(\rho) & \text{if } |\mathbf{D}'| = 0, \end{cases} \quad (26)$$

$$\text{div}(\mathbf{v}) \leq 0, \quad \begin{cases} p = -p_c(\rho) + \frac{F_0(2\eta(\rho)\sqrt{\text{div}(\mathbf{v})^2 + |\mathbf{D}'|^2}/F_0)^{1/n}}{\sqrt{\text{div}(\mathbf{v})^2 + |\mathbf{D}'|^2}} \text{div}(\mathbf{v}) & \text{if } \text{div}(\mathbf{v}) < 0, \\ p \geq -p_c(\rho) & \text{if } \text{div}(\mathbf{v}) = 0. \end{cases} \quad (27)$$

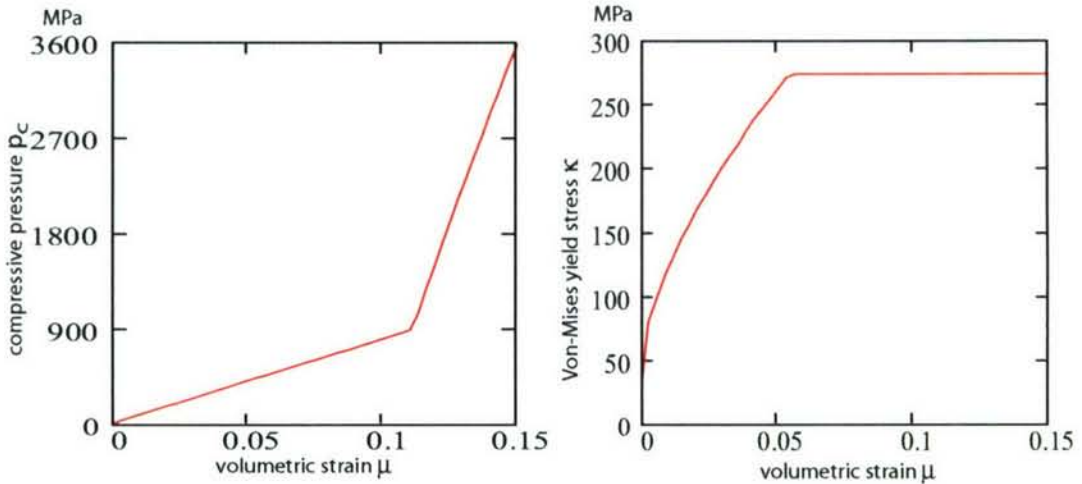


Figure 1: The dependence of p_c (left) and of the yield limit κ (right) with respect to the volumetric strain $\mu = \rho/\rho_0 - 1$ for concrete (data after [30]).

This model is an extension of Bingham type model (23) that captures the experimentally observed density changes under severe loadings. If we set $n = 1$, then we obtain:

$$\begin{cases} \boldsymbol{\sigma}' = \left[2\eta(\rho) + \frac{\kappa(\rho)}{|\mathbf{D}'|} \right] \mathbf{D}' & \text{if } |\mathbf{D}'| \neq 0, \\ |\boldsymbol{\sigma}'| \leq \kappa(\rho) & \text{if } |\mathbf{D}'| = 0, \end{cases} \quad (28)$$

$$\text{div}(\mathbf{v}) \leq 0, \quad \begin{cases} \text{trace}(\boldsymbol{\sigma})/3 = -p_c(\rho) + 2\eta(\rho)\text{div}(\mathbf{v}) & \text{if } \text{div}(\mathbf{v}) < 0 \\ \text{trace}(\boldsymbol{\sigma})/3 \geq -p_c(\rho) & \text{if } \text{div}(\mathbf{v}) = 0. \end{cases} \quad (29)$$

In what follows, the constitutive equation (28) will be referred to as the "revisited Bingham fluid".

In many solid-type models, p_c and κ are expressed as functions of the compaction level (or volumetric strain) $\mu = \rho/\rho_0 - 1$ instead of the density ρ (here ρ_0 is the density prior to loading). As an example, in Figure 1 is plotted a typical dependence of p_c and of the yield limit κ versus the compaction level μ for a concrete material (data and explicit expressions of these functions reported by Holmquist et al., 1993). The explicit expressions of these functions are given in section 5. Furthermore, the revisited Bingham fluid model can be recast in the form that is generally used in hydrocode calculations, by eliminating μ between $\kappa = \kappa(\mu)$ and $p_c = p_c(\mu)$. This type of dependence is also used in soil mechanics to eliminate the density as an unknown function. For the same concrete material, the obtained relation between the shear flow stress and pressure is represented in Figure 2.

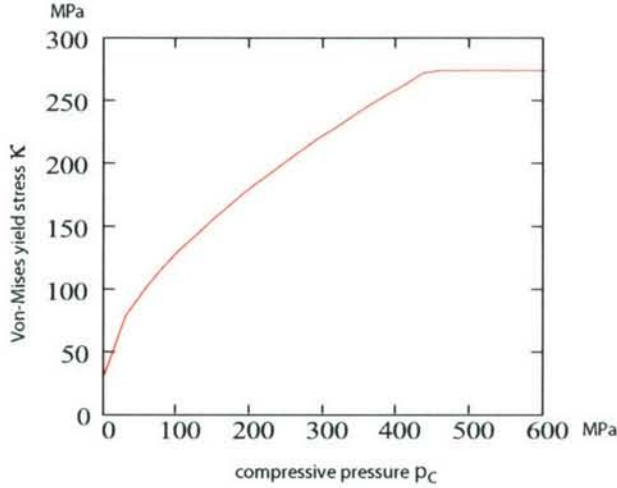


Figure 2: The dependence of the yield limit κ with respect to the pressure p for undamaged concrete (data after Holmquist et al., 1993).

2.3.3 Modified Cam-Clay fluid of Perzyna's type

As already mentioned, there is a critical need for developing constitutive models that could capture the complex rheological behavior of slurries and some oils. The fundamental question which arises concerns the flow pattern, particularly the shape and distribution of yielded/unyielded regions.

The Modified Cam-Clay yield function developed by Roscoe and Burland, 1968 captures very well commonly observed properties of soils such as compaction/dilatancy behavior and the tendency to eventually reach a state in which the volume becomes constant. Its adequacy has been tested against numerous experiments, the consensus being that it is most suitable for lightly overconsolidated particulate materials (for a review on the subject, see de Borst and Groen, 2000).

In view of applications to the description of the flow of slurries, we further examine whether a compressible viscoplastic fluid model compatible to a Modified Cam-Clay yield condition can be constructed using the viscoplastic regularization method.

The Modified Cam-clay yield condition is

$$F(p, q, \rho) = \sqrt{q^2/M^2 + (p + p_c(\rho))^2} - p_c(\rho),$$

where M is a constant. If we assume associated flow, the system (20) becomes

$$\begin{cases} \frac{F_0}{2\eta(\rho)} (F(p, q, \rho)/F_0)^n \frac{p + p_c(\rho)}{\sqrt{q^2/M^2 + (p + p_c(\rho))^2}} = d \\ \frac{F_0}{2\eta(\rho)} \sqrt{\frac{3}{2}} (F(p, q, \rho)/F_0)^n \frac{q/M^2}{\sqrt{q^2/M^2 + (p + p_c(\rho))^2}} = e. \end{cases}$$

In contrast to the above example (Mises yield condition), the system can be solved for all $(d, e) \in \mathbb{R} \times \mathbb{R}_+$, i.e. there are no kinematic restrictions $\mathcal{C} = \mathbb{R}_S^{3 \times 3}$. After some algebra, we obtain:

$$P(d, e, \rho) = -p_c(\rho) + d \frac{p_c(\rho) + F_0(2\eta(\rho)\sqrt{d^2 + 2M^2e^2/3}/F_0)^{1/n}}{\sqrt{d^2 + 2M^2e^2/3}},$$

$$Q(d, e, \rho) = \sqrt{\frac{2}{3}}M^2e \frac{p_c(\rho) + F_0(2\eta(\rho)\sqrt{d^2 + 2M^2e^2/3}/F_0)^{1/n}}{\sqrt{d^2 + 2M^2e^2/3}}.$$

Substitution in (65) leads to the following constitutive equation:

$$\left\{ \begin{array}{l} \boldsymbol{\sigma} = \left[-p_c(\rho) + \operatorname{div}(\mathbf{v}) \frac{p_c(\rho) + F_0(2\eta(\rho)\sqrt{\operatorname{div}(\mathbf{v})^2 + 2M^2|\mathbf{D}'(\mathbf{v})|^2/3}/F_0)^{1/n}}{\sqrt{\operatorname{div}(\mathbf{v})^2 + 2M^2|\mathbf{D}'(\mathbf{v})|^2/3}} \right] \mathbf{I} + \\ \quad \frac{2M^2}{3} \frac{p_c(\rho) + F_0(2\eta(\rho)\sqrt{\operatorname{div}(\mathbf{v})^2 + 2M^2|\mathbf{D}'(\mathbf{v})|^2/3}/F_0)^{1/n}}{\sqrt{\operatorname{div}(\mathbf{v})^2 + 2M^2|\mathbf{D}'(\mathbf{v})|^2/3}} \mathbf{D}'(\mathbf{v}) \quad \text{if } |\mathbf{D}(\mathbf{v})| \neq 0, \\ \quad F(p, q, \rho) \leq 0 \text{ if } |\mathbf{D}(\mathbf{v})| = 0. \end{array} \right. \quad (30)$$

The constitutive equation (30) describes a compressible fluid with flow behavior dependent on the first stress invariants and strain rate. If we set $n = 1$, we obtain the following simplified model

$$\left\{ \begin{array}{l} \boldsymbol{\sigma} = \left[-p_c(\rho) + \operatorname{div}(\mathbf{v}) \left(2\eta(\rho) + \frac{p_c(\rho)}{\sqrt{\operatorname{div}(\mathbf{v})^2 + 2M^2|\mathbf{D}'(\mathbf{v})|^2/3}} \right) \right] \mathbf{I} + \\ \quad \frac{2M^2}{3} \left[2\eta(\rho) + \frac{p_c(\rho)}{\sqrt{\operatorname{div}(\mathbf{v})^2 + 2M^2|\mathbf{D}'(\mathbf{v})|^2/3}} \right] \mathbf{D}'(\mathbf{v}) \quad \text{if } |\mathbf{D}(\mathbf{v})| \neq 0, \\ \quad F(p, q, \rho) \leq 0 \text{ if } |\mathbf{D}(\mathbf{v})| = 0. \end{array} \right. \quad (31)$$

2.4 Superposition method

In this section, we introduce a different procedure for determination of the explicit expressions of the functions $\alpha(d, e, \rho)$ and $\beta(d, e, \rho)$ involved in the general constitutive equation (65). The main assumption is that the state of stress in the material, $\boldsymbol{\sigma}$, can be represented as the sum of a viscous contribution $\boldsymbol{\sigma}^F$ and a contribution \mathbf{S} , related to plasticity effects, i.e.:

$$\boldsymbol{\sigma} = \boldsymbol{\sigma}^F + \mathbf{S}. \quad (32)$$

The viscous part of the stress is taken as for a classical viscous fluid,

$$\boldsymbol{\sigma}^F = \mathbf{f}^V(\mathbf{D}, \rho). \quad (33)$$

It should be noted that at difference with the stress-rate of deformation relation for a rigid viscoplastic fluid, the constitutive function \mathbf{f}^V is continuous and vanishes for $\mathbf{D} = 0$, i.e.

$$\mathbf{f}^V(\mathbf{D}, \rho) \rightarrow 0 = \mathbf{f}^V(0, \rho), \quad \text{for } \mathbf{D} \rightarrow 0, \quad (34)$$

For the sake of simplicity we shall consider only first order fluids

$$\mathbf{f}^V(\mathbf{D}, \rho) = \lambda(\mathbf{D}, \rho) \text{tr}(\mathbf{D}) \mathbf{I} + 2\eta(\mathbf{D}, \rho) \mathbf{D}, \quad (35)$$

where η and λ are viscosity coefficients which may depend on d, e and ρ , i.e. $\lambda = \lambda(d, e, \rho), \eta = \eta(d, e, \rho)$. For λ and η independent of d and e , i.e. $\lambda = \lambda(\rho), \eta = \eta(\rho)$, (33) reduces to the compressible Navier-Stokes model

$$\mathbf{f}^V(\mathbf{D}, \rho) = \lambda(\rho) d \mathbf{I} + 2\eta(\rho) \mathbf{D}, \quad (36)$$

but other choices can also be considered in (35). For example, for $\eta = B(\rho) \arg \sinh(Ae)/e$, with $A, B > 0$, we recover the Prandtl-Eyring type model and for $\eta = \mu(\rho)e^a$, with $a = 1/m - 1 > -1$, we obtain the Norton model. Models of isotropic fluids have been used to describe the slow motions of soils and glaciers on natural slopes (see Vulliet, 2000 for an overview on the subject).

We assume that there is flow only if a yield condition expressed in terms of \mathbf{S} and depending on ρ is satisfied (for a discussion concerning other choices of the hardening or damage parameters see last section). We further neglect second order effects in \mathbf{S} as well the influence of the third invariant of \mathbf{S} . Thus, the yield condition is expressed as $F(s, r, \rho) = 0$, where $s = \text{tr}(\mathbf{S})/3$ and $r = \sqrt{3/2} |\mathbf{S}'|$ are the first two invariants of \mathbf{S} . The deformation rate \mathbf{D} is then given by

$$\mathbf{D} = \Lambda [M(s, r, \rho) \mathbf{I} + N(s, r, \rho) \mathbf{S}'], \quad (37)$$

with $F(s, r, \rho) \leq 0$, $\Lambda \geq 0$ and $\Lambda F(s, r, \rho) = 0$, while M and N are scalar functions of their arguments. From (37) follows that for $\mathbf{D} \neq 0$, we obtain the following nonlinear system in the unknowns s, r and Λ

$$\begin{cases} 3\Lambda M(s, r, \rho) = d \\ \sqrt{\frac{2}{3}} \Lambda r N(s, r, \rho) = e \\ F(s, r, \rho) = 0. \end{cases} \quad (38)$$

Let us denote by $\mathcal{R}_F(\cdot, \cdot, \cdot, \rho) : \mathbb{R} \times \mathbb{R}_+ \times \mathbb{R}_+ \rightarrow \mathbb{R} \times \mathbb{R}_+$ the function defined by (38), i.e. $(e, d) = \mathcal{R}_F(s, r, \Lambda, \rho)$. The set of admissible rates of deformation \mathbf{D} is given by the image of the operator \mathcal{R}_F , i.e.

$$\mathcal{C} = \{ \mathbf{D} \in \mathbb{R}_S^{3 \times 3}; \exists (s, r, \Lambda) \text{ with } F(s, r, \rho) = 0, \text{ such that } (d, e) = \mathcal{R}_F(s, r, \Lambda, \rho) \}. \quad (39)$$

The invertibility of \mathcal{R}_F depends on the rank of the jacobian matrix of \mathcal{R}_F and $\dim(\mathcal{C})$. If (38) is invertible, i.e. for all $(d, e) \in \mathcal{C}$ we can solve the system (38) and there exist S, R and Λ such that

$$\begin{cases} s = S(d, e, \rho) \\ r = R(d, e, \rho) \\ \Lambda = \Lambda(d, e, \rho), \end{cases} \quad (40)$$

by combining (40), (32) and (35), we can obtain the explicit expressions for the constitutive functions α and β of (65):

$$\begin{cases} \alpha(d, e, \rho) = (\lambda(d, e, \rho) + \frac{2\eta(d, e, \rho)}{3})d + S(d, e, \rho), \\ \beta(d, e, \rho) = 2\eta(d, e, \rho) + \sqrt{\frac{2}{3}} \frac{R(d, e, \rho)}{e}. \end{cases} \quad (41)$$

As in the case when we make use of the Perzyna viscoplastic regularization method, we substitute the expressions (41) in the compatibility conditions (5)-(8). If one of these conditions is violated, we deduce that we cannot construct a fluid-type model (65) using the superposition method (32)-(37).

In the following, we construct fluid models using the superposition approach and compare their response with the viscoplastic fluid models presented in section 3. In some examples we shall assume an associated flow rule, i.e. that there exists a function $F(s, r, \rho)$ such that

$$M(\mathbf{S}, \rho) \mathbf{I} + N(\mathbf{S}, \rho) \mathbf{S}' = \frac{\partial F(\mathbf{S}, \rho)}{\partial \mathbf{S}}.$$

In such cases, the scalar scalar functions M, N are expressed as:

$$M(s, r, \rho) = \frac{1}{3} \frac{\partial F}{\partial s}(s, r, \rho), \quad N(s, r, \rho) = \frac{3}{2r} \frac{\partial F}{\partial r}(s, r, \rho). \quad (42)$$

2.4.1 Bingham Fluid

We first consider the superposition between a viscous fluid and a plastic solid obeying Mises yield condition, i.e. $F(s, r, \rho) = r \sqrt{\frac{2}{3}} - \kappa(\rho)$. If we assume associated flow (42), then (38) becomes

$$d = 0, \quad e = \Lambda, \quad r = \sqrt{\frac{3}{2}} \kappa(\rho).$$

This means that the flow is incompressible, i.e. the kinematic restriction coincides with (22). Moreover, s and α are undetermined while $R(d, e, \rho) = \sqrt{3/2} \kappa(\rho)$.

If we choose the compressible Navier-Stokes model (36) for the viscous part then $\beta(d, e, \rho) = 2\eta + \frac{k}{e}$, and we obtain the constitutive relation (24) of a Bingham fluid with yield limit dependent on density.

Let us note that if the flow-no flow condition is Von Mises yield function, using either method we obtain the classic Bingham fluid model. This is not the case for other yield conditions.

2.4.2 Bingham fluid, revisited

Next, we consider the superposition between a viscous fluid and a plastic solid that obeys the yield condition

$$F(s, r, \rho) = [\sqrt{2/3} r - \kappa(\rho)]_+ + [s + p_c(\rho)]_-,$$

where $[x]_+ = (|x| + x)/2$, $[x]_- = (|x| - x)/2$, and associated flow. The system (38) becomes

$$\begin{aligned} d = 0, \quad e = \Lambda & \quad \text{if } s > -p_c(\rho), r = \sqrt{3/2}\kappa(\rho), \\ d = -\Lambda, \quad e = 0 & \quad \text{if } s = -p_c(\rho), r < \sqrt{3/2}\kappa(\rho). \end{aligned}$$

If $s = -p_c(\rho)$ and $r = \sqrt{3/2}\kappa(\rho)$, we have to consider the normal cone to the plasticity surface and M and N are set valued functions, i.e.

$$d \leq 0, \quad e \geq 0, \quad \text{if } s = -p_c(\rho), r = \sqrt{3/2}\kappa(\rho).$$

The kinematic restriction is $\mathcal{C} = \{D ; \text{tr}(\mathbf{D}) \leq 0\}$, which implies that the flow is compressible and that unloading is rigid. Furthermore, for $|\mathbf{D}| \neq 0$ the system (38) can be inverted and we obtain:

$$S(d, e, \rho) = -p_c(\rho), \quad R(d, e, \rho) < \sqrt{\frac{3}{2}}\kappa(\rho), \quad \Lambda(d, e, \rho) = -d \quad \text{if } d < 0, e = 0,$$

$$S(d, e, \rho) > -p_c(\rho), \quad R(d, e, \rho) = \sqrt{\frac{3}{2}}\kappa(\rho), \quad \Lambda(d, e, \rho) = e \quad \text{if } d = 0, e > 0.$$

Substituting into (41) and choosing the compressible Navier-Stokes model (36) for the viscous part, we obtain the following constitutive equation:

$$\begin{cases} \boldsymbol{\sigma}' = \left[2\eta(\rho) + \frac{\kappa(\rho)}{|\mathbf{D}'|} \right] \mathbf{D}' & \text{if } |\mathbf{D}'| \neq 0 \\ |\boldsymbol{\sigma}'| \leq \kappa(\rho) & \text{if } |\mathbf{D}'| = 0, \end{cases} \quad (43)$$

$$\text{div}(\mathbf{v}) \leq 0, \quad \begin{cases} \text{trace}(\boldsymbol{\sigma})/3 = -p_c(\rho) + [\lambda(\rho) + 2\eta(\rho)/3]\text{div}(\mathbf{v}) & \text{if } \text{div}(\mathbf{v}) < 0 \\ \text{trace}(\boldsymbol{\sigma})/3 \geq -p_c(\rho) & \text{if } \text{div}(\mathbf{v}) = 0. \end{cases} \quad (44)$$

Let us note that this model is different from the constitutive equation (28)-(29) obtained using Perzyna's approach. The difference stands in the viscous terms of the spherical part of the stress.

Under hydrostatic conditions, most cementitious materials show a highly non-linear pressure-volumetric strain response, the reversible decrease in volume being very small. The experimental observations also suggest that in the high-pressure regime, a very large increase in pressure is necessary in order to produce even a very small change in density. Thus, the hypothesis of a "locking medium" can be made, i.e. the density cannot exceed a critical value. This critical density ρ^* , called locking density, corresponds to a state in the material when all the pores and micro-cracks are closed. The pressure level at which this density is first reached, called locking pressure, is denoted by $p^* = p_c(\rho^*)$. Hence, for such materials a pressure-density relationship of the following form could be considered:

$$\begin{cases} p = p_c(\rho), & \text{if } \rho < \rho^* \\ p \geq p^*, & \text{if } \rho = \rho^*. \end{cases} \quad (45)$$

2.4.3 Superposed Cam-Clay fluid

Next, we consider the superposition between a viscous fluid and a plastic solid that obeys the Modified Cam-clay yield condition $F(s, r, \rho) = \sqrt{r^2/M^2 + (s + p_c(\rho))^2} - p_c(\rho)$ and an associated flow rule. The system (38) becomes

$$d = \Lambda \frac{s + p_c(\rho)}{p_c(\rho)}, \quad e = \Lambda \sqrt{\frac{3}{2}} \frac{r}{M^2 p_c(\rho)}, \quad \frac{r^2}{M^2} + (s + p_c(\rho))^2 = p_c^2(\rho)$$

This algebraic system can be solved for all $(d, e) \in \mathbb{R} \times \mathbb{R}_+$, (i.e. there are no kinematic conditions $\mathcal{C} = \mathbb{R}_S^{3 \times 3}$) and after some algebra we get:

$$S(d, e, \rho) = -p_c(\rho) + d \frac{p_c(\rho)}{\sqrt{d^2 + 2M^2 e^2 / 3}}, \quad R(d, e, \rho) = \sqrt{\frac{2}{3}} M^2 e \frac{p_c(\rho)}{\sqrt{d^2 + 2M^2 e^2 / 3}}.$$

Finally, if the compressible Navier-Stokes model (36) for the viscous part is chosen, we deduce the constitutive equation

$$\begin{cases} \boldsymbol{\sigma} = \left[-p_c(\rho) + \text{div}(\mathbf{v}) \left(\lambda(\rho) + \frac{2\eta(\rho)}{3} + \frac{p_c(\rho)}{\sqrt{\text{div}(\mathbf{v})^2 + 2M^2 |\mathbf{D}'(\mathbf{v})|^2 / 3}} \right) \right] \mathbf{I} + \\ \left[2\eta(\rho) + \frac{2}{3} M^2 \frac{p_c(\rho)}{\sqrt{\text{div}(\mathbf{v})^2 + 2M^2 |\mathbf{D}'(\mathbf{v})|^2 / 3}} \right] \mathbf{D}'(\mathbf{v}) & \text{if } |\mathbf{D}(\mathbf{v})| \neq 0, \\ F(p, q, \rho) \leq 0 & \text{if } |\mathbf{D}(\mathbf{v})| = 0. \end{cases} \quad (46)$$

Let us note that the above constitutive equation for the Cam-clay fluid, obtained using the superposition method, is slightly different from (31) which was constructed

using Perzyna's approach and a static yield condition of the same functional form. In both models, the part of the stress which is rate independent is the same, and only the viscous contribution is different.

2.4.4 CAP fluid

Cap models are among the most widely used models for the description of the mechanical behavior of soils. We examine herein whether a cap yield condition can be used to construct a viscoplastic fluid-type model using the superposition method. Thus, we superpose a viscous fluid on a plastic solid satisfying a cap plasticity yield condition with a modified Drucker-Prager envelope (see Katona, 1984), i.e. we consider that the yield surface is divided into three regions along the s -axis (s being the first invariant of the plastic component of the stress tensor): the failure surface region $3s \in (-L(\rho), T)$; the cap surface region $3s \in (-X(\rho), -L(\rho))$ and the tension cut-off region ($3s \geq T$). We consider the failure surface to be of a modified Drucker-Prager form (see Katona, 1984), i.e. $r/\sqrt{3} + C \exp(3Bs) - A$, where A and C are constants ($A > C$). It constitutes a boundary along which the cap surface can move (harden or soften). The cap surface is a hardening surface in the shape of an ellipse when plotted in the space $(r, -s)$ (see Figure 3). It is defined as $\frac{1}{f_0} \left[r^2/3 - \frac{(X(\rho) - L(\rho))^2 - (3s - L(\rho))^2}{R_0^2} \right]$. The variable cap parameters L and X are positions on the s axis which locate the current cap surface, while the parameter R defines the ratio of the principal ellipse radii. The tension-cutoff criterion is triggered when $s > T$, whereas T is a material constant representing the threshold of hydrostatic tensile stress at which abrupt stress release occurs due to tension damage. Thus, we consider

$$F(s, r, \rho) = \begin{cases} 3s - T, & \text{if } 3s \geq T \\ r/\sqrt{3} + C \exp(3Bs) - A, & \text{if } -L(\rho) \leq 3s \leq T \\ \frac{1}{f_0} \left[r^2/3 - \frac{(X(\rho) - L(\rho))^2 - (3s - L(\rho))^2}{R_0^2} \right], & \text{if } -X(\rho) \leq 3s \leq -L(\rho), \end{cases} \quad (47)$$

and an associated flow rule (see a depiction of the yield surface on Figure 3 (left)). Then the system (38) becomes

$$\begin{cases} d = 3\Lambda e = 0 & \text{if } s = T/3, r \in [0, r_T], \\ d = 3\Lambda BC \exp(3Bs), e = \Lambda/\sqrt{2} & \text{if } 3s \in (-L(\rho), T), r = \sqrt{3}(A + C \exp(3Bs)) \\ d = \frac{6}{f_0 R_0^2} \Lambda (3s - L(\rho)), e = \sqrt{\frac{2}{3}} \Lambda \frac{1}{f_0} r & \text{if } 3s \in (-X(\rho), -L(\rho)), F(s, r, \rho) = 0 \end{cases} \quad (48)$$

if the stress point (s, r) is on the smooth part of the plastic surface $F(s, r, \rho) = 0$. In the two singular corner regions $3s = T, r = R_T$ and $3s = -L(\rho), r = R_L(\rho)$ (see

figure 3 left) the gradient of F is set valued and we have

$$\begin{cases} 3\Lambda BC \exp(BT) \leq d \leq 3\Lambda, 0 \leq e \leq \Lambda/\sqrt{2} & \text{if } 3s = T, r = R_T, \\ 0 \leq d \leq 3\Lambda BC \exp(-BL(\rho)), \Lambda/\sqrt{2} \leq e \leq \sqrt{\frac{2}{3}}\Lambda \frac{1}{f_0} R_L(\rho), & \text{if } 3s = -L(\rho), r = R_L(\rho) \end{cases} \quad (49)$$

The above algebraic system can be solved for all $(d, e) \in \mathbb{R} \times \mathbb{R}_+$, (i.e. there are no kinematic conditions $\mathcal{C} = \mathbb{R}_S^{3 \times 3}$) and after some algebra, we get:

$$\begin{cases} S(d, e, \rho) = T/3, R(d, e, \rho) = R_T & \text{if } d/e \geq 3\sqrt{2}BC \exp(BT), \\ S(d, e, \rho) = \frac{1}{3B}[\ln(d/e) - \ln(3\sqrt{2}BC)], & \\ R(d, e, \rho) = \sqrt{3}[A - \frac{1}{3\sqrt{2}B}d/e] & \text{if } 3\sqrt{2}BC \exp(BT) \geq d/e \geq 3\sqrt{2}BC \exp(-BL(\rho)), \\ S(d, e, \rho) = -L(\rho)/3, R(d, e, \rho) = R_L(\rho), & \text{if } 3\sqrt{2}BC \exp(-BL(\rho)) \geq d/e \geq -\sqrt{\frac{2}{3}}\frac{18L(\rho)}{R_0^2 R_L(\rho)} \\ S(d, e, \rho) = L(\rho)/3 + R_0 \sqrt{\frac{3}{2}} \frac{(X(\rho) - L(\rho))d}{27\sqrt{e^2/3 + R_0^2 d^2/54}}, & \\ R(d, e, \rho) = \frac{(X(\rho) - L(\rho))e}{R_0 \sqrt{e^2/3 + R_0^2 d^2/54}} & \text{if } -\sqrt{\frac{2}{3}}\frac{18L(\rho)}{R_0^2 R_L(\rho)} \geq d/e. \end{cases} \quad (50)$$

Finally, we arrive at the following cap fluid type model

$$\begin{cases} \boldsymbol{\sigma} = \left[\operatorname{div}(\mathbf{v}) \left(\lambda(\rho) + \frac{2\eta(\rho)}{3} \right) + S(\operatorname{div}(\mathbf{v}), |\mathbf{D}'(\mathbf{v})|, \rho) \right] \mathbf{I} + \\ \left[2\eta(\rho) + \sqrt{\frac{2}{3}} \frac{R(\operatorname{div}(\mathbf{v}), |\mathbf{D}'(\mathbf{v})|, \rho)}{|\mathbf{D}'(\mathbf{v})|} \right] \mathbf{D}'(\mathbf{v}) & \text{if } |\mathbf{D}(\mathbf{v})| \neq 0, \\ F(p, q, \rho) \leq 0 & \text{if } |\mathbf{D}(\mathbf{v})| = 0, \end{cases} \quad (51)$$

if the compressible Navier-Stokes model (36) for the viscous part is chosen.

2.5 It does not always work

As mentioned previously, it is not always possible to obtain consistent viscoplastic fluid formulations starting from any two-invariant yield functions. A first example is given below.

Let $F(p, q, \rho) = q + p \tan(\beta) - \kappa_0(\rho)$, i.e. Drucker-Prager yield condition with constant angle of friction β and cohesion κ_0 dependent on the density. We take $\phi(x) = ([x]_+/F_0)^n$ and further assume non-associated flow, i.e. $A(p, q, \rho) = F_0 \partial_p G(p, q)/3$ and $B(p, q) = 3F_0 \partial_q G(p, q)/(2q)$. It follows that

$$d = \frac{F_0}{2\eta(\rho)}([F(p, q, \rho)]_+/F_0)^n \frac{\partial G}{\partial p}(p, q), \quad e = \sqrt{\frac{3}{2}} \frac{F_0}{2\eta(\rho)}([F(p, q, \rho)]_+/F_0)^n \frac{\partial G}{\partial q}(p, q).$$

If the potential is chosen of the form $G(p, q) = q + p \tan(\psi)$, where the constant ψ is the dilation angle, then from the above equation, we deduce that $d = \sqrt{2/3} \tan(\psi) e$.

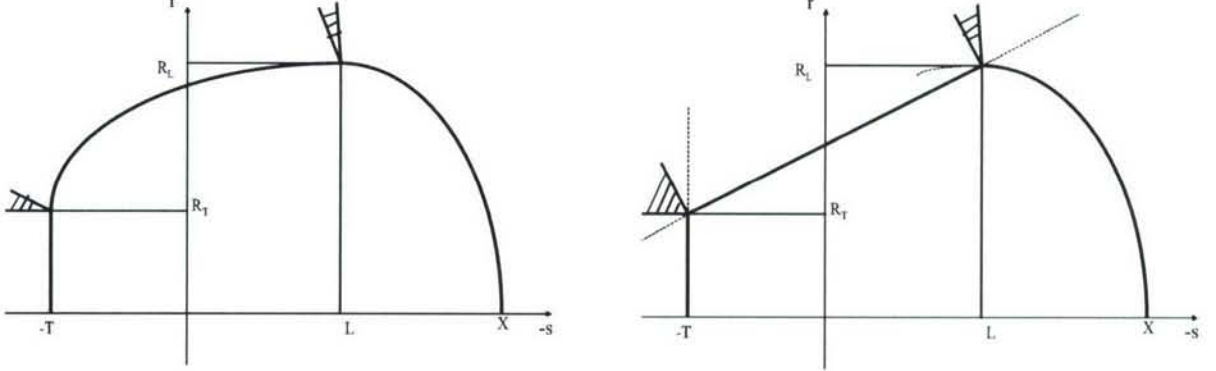


Figure 3: Schematic representation. Left: the cap plasticity condition with a modified Drucker-Prager form used for the cap fluid (51). Right: the cap plasticity condition with a standard Drucker-Prager surface which violates the continuity condition (6). The shaded areas are "singular corner regions".

This means that the set of admissible deformation rates is:

$$\mathcal{C} = \{\mathbf{D} \in \mathbb{R}_S^{3 \times 3} ; \operatorname{tr}(\mathbf{D}) = \sqrt{\frac{2}{3}} \tan(\psi) |\mathbf{D}'| \}. \quad (52)$$

This kinematic constraint is rather artificial and severely limits the flow. Moreover, reinforcing such a constraint would pose insurmountable numerical problems.

If we use for the flow potential another well-accepted expression (e.g. see [2]) $G(p, q) = \sqrt{q^2 + l_0^2} + p \tan(\psi)$, where l_0 and ψ are constants, we obtain:

$$d = \sqrt{2/3} \tan(\psi) e \sqrt{1 + (l_0/q)^2},$$

which implies the following kinematic admissible set

$$\mathcal{C} = \{\mathbf{D} \in \mathbb{R}_S^{3 \times 3} ; \operatorname{tr}(\mathbf{D}) \geq \sqrt{\frac{2}{3}} \tan(\psi) |\mathbf{D}'| \}. \quad (53)$$

As in the previous case, the resulting kinematic constraints restrict drastically the flow and are very difficult to justify or handle numerically.

Concerning the Cap fluid model (51), it is worth noting that even though the plasticity condition is specified in terms of three functions, the inverse functions

S and R are continuous in $\mathbb{R} \times \mathbb{R}_+ \setminus \{(0, 0)\}$. This is a direct consequence of the choice of an exponential dependence on the first invariant instead of the standard Drucker-Prager expression of the envelope. Next, we show that if the standard Drucker-Prager envelope is used then the response functions R, S are discontinuous, which is physically unacceptable.

Indeed, if in the cap plasticity condition (47), with associated flow rule, we take (see [20]) the standard Drucker-Prager expression for the envelope, i.e.:

$$F(s, r, \rho) = r/\sqrt{3} + 3Bs - A \text{ if } -L(\rho) \leq 3s \leq T. \quad (54)$$

(see also Figure 3 (right) then, after some algebra, we find that there are no kinematic conditions, $\mathcal{C} = \mathbb{R}_S^{3 \times 3}$, and we obtain the following expressions of S and R instead of (50):

$$\begin{cases} S(d, e, \rho) = T/3, R(d, e, \rho) = R_T & \text{if } d/e > 3\sqrt{2}/B, \\ S(d, e, \rho) = -L(\rho)/3, R(d, e, \rho) = R_L(\rho) & \text{if } 3\sqrt{2}/B > d/e \geq -\sqrt{\frac{2}{3}} \frac{18L(\rho)}{R_0^2 R_L(\rho)}, \\ S(d, e, \rho) = L(\rho)/3 + R_0 \sqrt{\frac{3}{2}} \frac{(X(\rho) - L(\rho))d}{27\sqrt{e^2/3 + R_0^2 d^2/54}}, \\ R(d, e, \rho) = \frac{(X(\rho) - L(\rho))e}{R_0 \sqrt{e^2/3 + R_0^2 d^2/54}}, & \text{if } -\sqrt{\frac{2}{3}} \frac{18L(\rho)}{R_0^2 R_L(\rho)} \geq d/e \end{cases} \quad (55)$$

Note that the functions S and R have a discontinuity on the line $d = 3\sqrt{2}e/B$ of the $d - e$ plane. From (41) it follows that the constitutive functions α and β have the same discontinuity with respect to \mathbf{D} , which violates the compatibility condition (6).

2.6 Examples of the models' response

We illustrate the response of the models proposed for uniaxial strain compression conditions. Suppose that in the reference configuration the material sample occupies the cylinder $C_0 = (0, L_0) \times \omega$. In the deformed configuration at time t , the material sample occupies $C_t = (0, L(t)) \times \omega$ (see Figure 4 top). The deformation is supposed to be homogeneous $x = L(t)X/L_0$, $y = Y$, $z = Z$ and the velocity in Eulerian coordinates x, y, z is $v_x = \dot{L}(t)x/L(t)$, $v_y = 0$, $v_z = 0$, so the only non-zero component of the rate of deformation tensor is $D_{xx} = \dot{L}(t)/L(t)$.

If we denote by ρ_0 , the density at $t = 0$, then at any time $t > 0$, the density ρ , the compaction factor (volumetric strain) $\mu = \rho/\rho_0 - 1$, and the invariants of \mathbf{D} are given by

$$\rho(t) = \frac{L(t)}{L_0} \rho_0, \quad \mu(t) = \frac{L_0}{L(t)} - 1, \quad d(t) = \frac{1}{3} \frac{\dot{L}(t)}{L(t)}, \quad e(t) = \sqrt{\frac{2}{3}} \frac{|\dot{L}(t)|}{L(t)}.$$

This loading process corresponds to compression of the sample material in the x direction (see Figure 4 top).

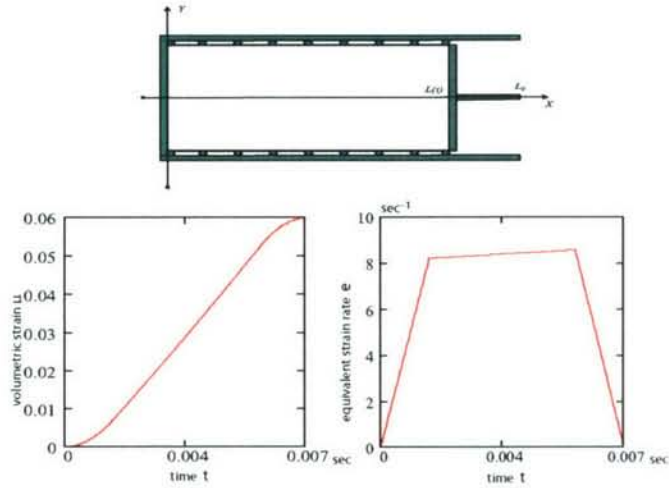


Figure 4: The evolution of the compaction factor $t \rightarrow \mu(t)$ (left) and of the equivalent strain rate $t \rightarrow e(t)$ (right) for the second loading history.

Let us consider the following loading history: the piston which at $t = 0$ has the velocity $V(0) = 0$, uniformly accelerates in the time interval $t \in [0, t_0]$ to reach a constant velocity value V , which is kept constant for $t \in [t_0, t_0 + T]$, i.e. $V(t) = V$ and then uniformly decelerates to reach a vanishing velocity at $t = T + 2t_0$. That means that the velocity of the piston is given by $\dot{L}(t) = -tV/t_0$ for $t \in [0, t_0]$, $\dot{L}(t) = -V$ for $t \in [t_0, t_0 + T]$ and $\dot{L}(t) = -V(T + 2t_0 - t)/t_0$.

To examine the capability of the proposed models to describe high-strain rate effects, we compare the response of each material for three different velocities: $V/L_0 = 10\text{s}^{-1}$, $V/L_0 = 100\text{s}^{-1}$ and $V/L_0 = 1000\text{s}^{-1}$. We choose the constants t_0 and T such as to ensure that the final compaction level $\mu_{final} = 0.06$ reached in each experiment is the same (i.e. we take $t_0 = 1/240\text{s}$, $T = 1/80\text{s}$ for the first experiment, $t_0 = 1/2400\text{s}$, $T = 1/800\text{s}$ for the second and $t_0 = 1/24000\text{s}$, $T = 1/8000\text{s}$ for the third one). As an example, the evolution of the volumetric strain $t \rightarrow \mu(t)$ and of the equivalent strain rate $t \rightarrow e(t)$ for the second loading history, are plotted in Figure 4. Note that in the Eulerian description the strain rate is not constant on $t \in [t_0, t_0 + T]$ even if the piston has a constant velocity.

2.6.1 Bingham fluid, revisited

First, we consider the revisited Bingham fluid model (68)-(69). The specific expressions of the constitutive functions $\kappa(\rho)$ and $p_c(\rho)$, taken from Holmquist et al. (1993), correspond to a concrete material (see also Figure 1 for plot of these functions). The function p_c is expressed in terms of the volumetric strain $\mu = \rho/\rho_0 - 1$ as: $p_c(\mu) = \mu p_{crush}/\mu_{crush}$ if $\mu \leq \mu_{crush}$, $p_c(\mu) = p_{crush} + (\mu - \mu_{crush})(p_{lock} - p_{crush})/(\mu_{lock} - \mu_{crush})$

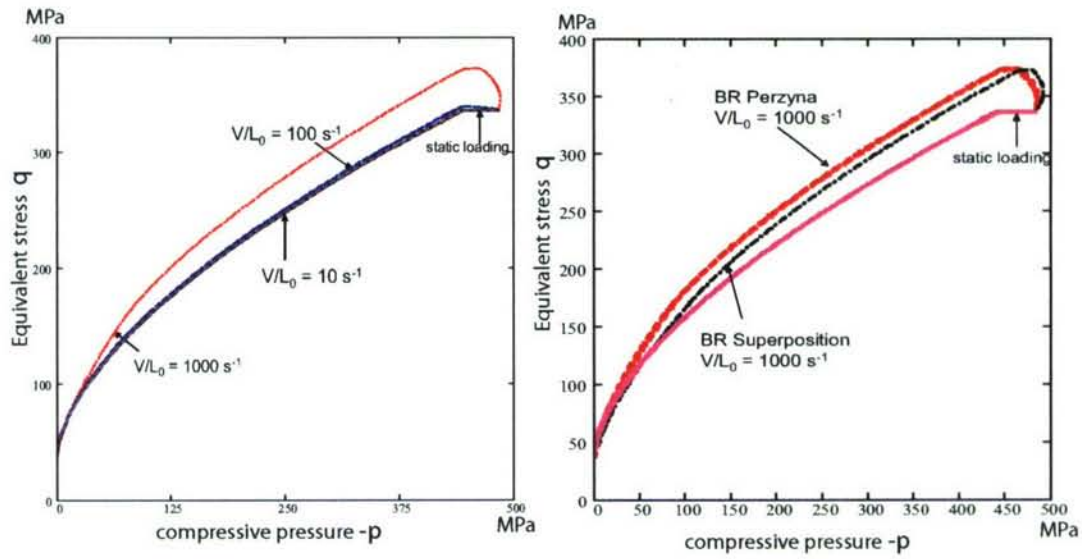


Figure 5: Left: the stress evolution $t \rightarrow (-p(t), q(t))$ of the revisited Bingham model (68)-(69) for three loading histories. Right: a comparison between the stress evolution $t \rightarrow (-p(t), q(t))$ for the two revisited Bingham (BR) models, (28)-(29) obtained using the Perzyna approach and (68)-(69) obtained using superposition approach, and for $V/L_0=1000/s$.

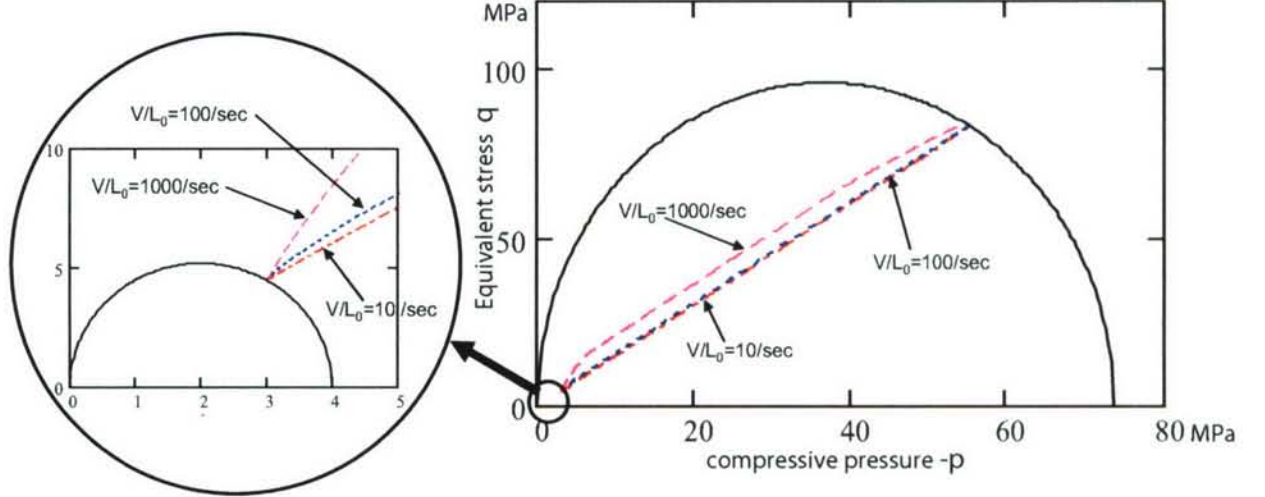


Figure 6: Right: the stress evolution $t \rightarrow (-p(t), q(t))$ of the Cam-clay fluid (31) for three loading histories. The solid line represents the final plastic surface, i.e. $F(p, q, \mu_{fin}) = 0$. Left: the very beginning of the stress path. The solid line represents here the initial plastic surface, i.e. $F(p, q, 0) = 0$.

if $\mu \in [\mu_{crush}, \mu_*]$ and $p_c(\mu) = K_1(\mu - \mu_{lock})/(1 + \mu_{lock}) + K_2[(\mu - \mu_{lock})/(1 + \mu_{lock})]^2 + K_3[(\mu - \mu_{lock})/(1 + \mu_{lock})]^3$ if $\mu \geq \mu_*$. The specific values are $p_{crush} = 16$ MPa, $p_{lock} = 800$ MPa, $\mu_{crush} = 0.001$, $\mu_{lock} = 0.1$, $\mu_* = 0.111$ and $K_1 = 85000$ MPa, $K_2 = -171000$ MPa, $K_3 = 208000$ MPa. The function $\kappa(\mu)$ depends on μ through $p_c(\mu)$ (see Figure 2)

$$\kappa(\mu) = \sigma_0 \sqrt{2/3} \min\{S_{max}, A + B(p_c(\mu)/\sigma_0)^N\} \quad (56)$$

with $\sigma_0 = 48$ MPa, $S_{max} = 7$, $A = 0.79$, $B = 1.60$, $N = 0.61$. The viscosity coefficients were supposed to be constants $\lambda = 0.002$ MPas, $\eta = 0.001$ MPas.

In Figure 5 (left) is shown the evolution of the stress in the $q - p$ plane for the three loading rates considered. For the test at $(V/L_0 = 10/s)$ and $(V/L_0 = 100/s)$, the stress curves are very close to the static curve $q = \sqrt{3/2}\kappa(p)$. A larger difference with respect to the static response is observed in the third experiment $(V/L_0 = 1000/s)$.

A comparison between the revisited Bingham (BR) models obtained using the Perzyna approach (28)-(29) and the superposition method (68)-(69) is presented in Figure 5 (right) for $V/L_0 = 1000/s$. The rate effects as well as the difference in response between the two models is clearly observed.

2.6.2 Cam-clay fluid

We apply the Cam-clay fluid (31) obtained using Perzyna approach to a shale (data after Niandou, 1994). The expression of p_c is: $p_c(\mu) = p_0(1+\mu)^{1/l}$ which corresponds to an oily shale sample (Tournemire, France). The material constants are: $M = 2.6$, $p_0 = 2$ MPa, $l=0.02$ and the viscosity coefficient is supposed to be constant $\eta = 0.01$ MPas.

In Figure 6 (right) we have plotted the evolution of the stress in the $q-p$ plane for the three loading rates. The final plastic surface, i.e. $F(p, q, \mu_{fin}) = 0$ is represented by a solid line. For the first two loading rates $V/L_0 = 10/s$ and $V/L_0 = 100/s$, the response is very close. Some difference in response is observed for an order of magnitude increase in the loading rate ($V/L_0 = 1000/s$). Figure 6 (left) shows the beginning of the loading process. In this figure, the solid line represents the initial plastic surface, i.e. $F(p, q, 0) = 0$. The rate effects on the flow are clearly observed. Although all the stress curves start from the initial plastic surface, their evolution is different, the most pronounced difference being between the response corresponding to the lowest and highest loading rates.

2.7 On the choice of internal parameters

In all the models presented, the assumption was made that the only dissipative mechanism is plastic flow and the associated internal variable is either the density ρ or the porosity/compaction level μ . Although the choice of the density as hardening parameter is physically sound and very suitable for an Eulerian description of large deformation and high strain rate behavior, a more realistic description of the irrecoverable deformation should also account for coupling between plasticity, damage and viscous effects. A discussion of other choices for internal variables is given in this section.

We denote by $\mathbf{h} \in \mathbb{R}^n$ the vector of n scalar internal parameters in the Eulerian description. All the constitutive functions F , α and β will depend also on the internal vector \mathbf{h} and the constitutive equation (65) becomes

$$\mathbf{D}(\mathbf{v}) \in \mathcal{C}, \quad \begin{cases} \boldsymbol{\sigma} = \alpha(\mathbf{D}(\mathbf{v}), \mathbf{h})\mathbf{I} + \beta(\mathbf{D}(\mathbf{v}), \mathbf{h})\mathbf{D}'(\mathbf{v}) & \text{if } |\mathbf{D}(\mathbf{v})| \neq 0, \\ F(\boldsymbol{\sigma}, \mathbf{h}) \leq 0 & \text{if } |\mathbf{D}(\mathbf{v})| = 0, \end{cases} \quad (57)$$

We complete the model (57) by providing the evolution equation for the internal variable \mathbf{h} . We assume that the total (particular) derivative of \mathbf{h} is a function of \mathbf{h} and the stretch tensor, i.e.

$$\frac{d\mathbf{h}}{dt} = \frac{\partial \mathbf{h}}{\partial t} + \mathbf{v} \cdot \nabla \mathbf{h} = \mathbf{H}(\mathbf{D}, \mathbf{h}). \quad (58)$$

If \mathbf{H} is isotropic with respect to \mathbf{D} then it depends on \mathbf{D} through its invariants. For simplicity, we further suppose that \mathbf{H} is a function of only the first two invariants of \mathbf{D} , i.e. $\mathbf{H} = \mathbf{H}(d, e, \mathbf{h})$.

A first choice for the description of hardening parameter is the density ρ . In this way, we capture the effect of pore closing/collapse on the response of geological/cementitious materials. If we set $n = 1$ and $\mathbf{h} = \rho$ then the evolution equation for the hardening parameter (66) reduces to the continuity equation (12), and $\mathbf{H} = H(d, e, \rho) = -\rho d$. In many applications, the volumetric (plastic) strain $\mu = \rho/\rho_0 - 1$, is used instead of the density. In this case (66) becomes

$$\frac{d\mu}{dt} = \frac{\partial\mu}{\partial t} + \mathbf{v} \cdot \nabla\mu = -(1 + \mu)d, \quad (59)$$

and $\mathbf{H} = H(d, e, \mu) = -(\mu + 1)d$.

Other authors (e.g. Cristescu and Hunsche, 1998) use as hardening parameter the visco-plastic work per unit volume w , i.e. $n = 1$, $\mathbf{h} = w$, where $\dot{w} = \boldsymbol{\sigma} : \mathbf{D}$. From (57) we deduce

$$\frac{dw}{dt} = \frac{\partial w}{\partial t} + \mathbf{v} \cdot \nabla w = \alpha(d, e, w)d + \beta(d, e, w)e^2, \quad (60)$$

with $\mathbf{H} = H(d, e, w) = \alpha(d, e, w)d + \beta(d, e, w)e^2$.

To capture the combined effect of plasticity and damage, we propose the following extension of the revisited Bingham model (68)-(29):

$$\begin{cases} \boldsymbol{\sigma}' = \left[2\eta + \frac{\kappa(\mu, \delta)}{|\mathbf{D}'|} \right] \mathbf{D}' & \text{if } |\mathbf{D}'| \neq 0 \\ |\boldsymbol{\sigma}'| \leq \kappa(\rho, \delta) & \text{if } |\mathbf{D}'| = 0, \end{cases} \quad (61)$$

$$div(\mathbf{v}) \leq 0, \quad \begin{cases} tr(\boldsymbol{\sigma})/3 = -p_c(\mu) + (\lambda + 2\eta/3)div(\mathbf{v}) & \text{if } div(\mathbf{v}) < 0 \\ tr(\boldsymbol{\sigma})/3 \geq -p_c(\mu) & \text{if } div(\mathbf{v}) = 0, \end{cases} \quad (62)$$

with two internal parameters: the volumetric strain μ and a scalar damage parameter δ . The damage parameter is associated to the loss of cohesive strength due to air pore collapse. Following Holmquist et al. (1993), we consider that the shear flow stress is of the form

$$\kappa(\mu, \delta) = \sigma_0 \sqrt{2/3} \min\{S_{max}, A(1 - \delta) + B(p_c(\mu)/\sigma_0)^N\}. \quad (63)$$

The function $p_c(\mu)$, is plotted in Figure 1 (expression given in section 6.1).

The evolution equation for μ is (59) while for the damage parameter we consider

$$\frac{d\delta}{dt} = \frac{\partial\delta}{\partial t} + \mathbf{v} \cdot \nabla\delta = \frac{e}{\Delta(\mu)}, \quad (64)$$

with $\Delta(\mu) = \sqrt{2/3} \max\{r_0, D_1[(p_c(\mu) + T)/\sigma_0]^{D_2}\}$. Note that these evolution equations can be written in the form (66) with $n = 2$, $\mathbf{h} = (\mu, \delta)$ and $\mathbf{H}(d, e, \mathbf{h}) = (-(1 + \mu)d, e/\Delta(\mu))$.

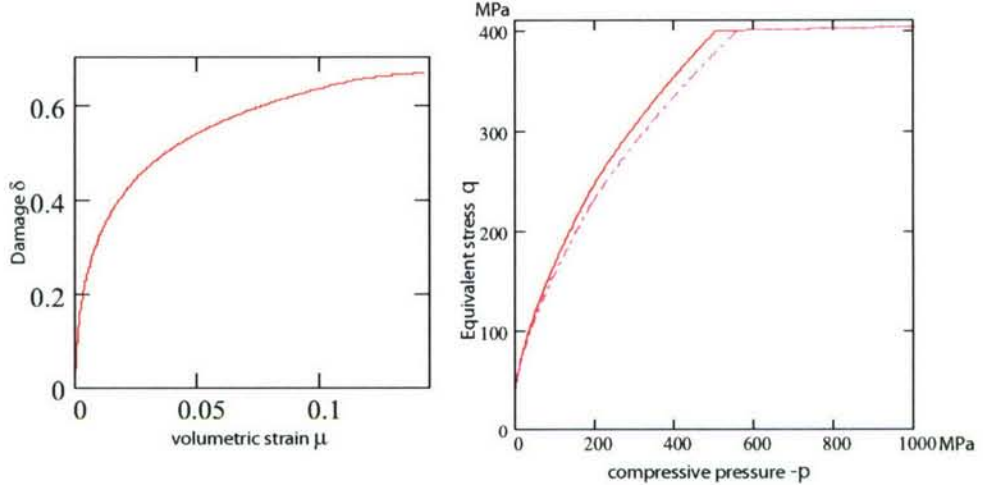


Figure 7: Left: the evolution of the internal parameters $t \rightarrow (\mu(t), \delta(t))$). Right: the evolution of the stress $t \rightarrow (-p(t), q(t))$ during the second experiment ($V/L_0 = 100/\text{sec}$) for the model with damage (dashed line) and without damage (solid line).

We further illustrate the response of this model for concrete subject to uniaxial compression conditions. The law of variation of $p_c(\mu)$ is taken as that reported by Holmquist et al. (1993), which was given in the previous section (see also Figure 1). We take $r_0 = 0.01$, $D_1 = 0.04$, $D_2 = 1$. and for the tension cut-off pressure T (see 51, we take the value reported in Holmquist et al. (1993), i.e. $T = 4. MPa$. In Figure 7 (left) is shown the evolution of the damage as a function of the compaction level μ for the loading rate $V/L_0 = 100/s$ as in the second experiment but with $\mu_{fin} = 0.15$. Note that during loading, damage is continuously increasing until it reaches the value $\delta_{fin} = 0.6$. Figure 7 (right) shows in the $p - q$ plane, the stress variation during the same test ($V/L_0 = 100/s$) in the case as described by the revisited Bingham model with damage (dashed line) and without damage (solid line). As expected, the presence of damage causes a decrease in the yield stress.

2.8 Conclusions

A general methodology for constructing fluid-type constitutive equations for description of the combined effects of plasticity, damage and viscous effects on the behavior of cementitious and particulate media when subjected to large deformations and high strain rates was proposed. The elastic deformations were neglected and the representation of the dynamic state of stress in the material was obtained from classical yield conditions for plastic solids using two methods: (1) the viscoplastic regularization and (2) a Maxwell type stress superposition method. Examples of constitutive equations obtained from classical two-invariant yield conditions F using

both procedures are presented. In general, even if we start from the same yield condition, the models obtained using these two methods are different. In the case of the Mises yield condition which is a function only of the second invariant, using either model we obtain the classical Bingham fluid model. To better capture the behavior of porous geological or cementitious materials under severe loadings (high-pressure, high strain rate behavior), extensions of the Bingham classical model were proposed using both procedures. Those rigid viscoplastic fluid models are compressible, their flow-no flow threshold and subsequent flow behavior being dependent on the density or compaction level.

We showed that for some yield conditions F , certain kinematic restrictions need to be satisfied. In the case of the Mises yield condition, the kinematic constraint that ought to be fulfilled is the incompressibility condition. However, for certain classical yield functions, such as Drucker-Prager the resulting kinematic constraints are physically unacceptable and we cannot arrive at consistent rigid-viscoplastic fluid type formulations. For other yield conditions, such as the Cap model with a standard Drucker-Prager envelope, the derived fluid-type model has discontinuities with respect to the deformation rate, which makes the model inconsistent.

We illustrated the response of the proposed models for uniaxial compression conditions and compared their respective responses.

Extensions of these models that include coupling between damage, plastic and viscous effects are proposed and their predictive capabilities and limitations were discussed.

References

- [1] Alexandrou, A.N., Le Menn, P., Georgiou, G., Entov, V., 2003. Flow instabilities of Herschel-Bulkley fluids, *J. Non-Newtonian Fluid Mech.* 116, 19–32.
- [2] ABAQUS,2003. Analysis user's manual, vol (iii), Materials, ABAQUS Inc.
- [3] Batra, R.C., 1987. Steady-state penetration of viscoplastic targets, *Int. J. Engng. Sci.* 25, 1131–1141.
- [4] Batra, R.C., Lin, P-R., 1988. Steady-state deformations of a rigid perfectly plastic rod striking a rigid cavity, *Int. J. Engng. Sci.* 26, 183–192.
- [5] Campbell, C.S., Brennen, C.E.,1985. Computer simulation of granular shear flows. *J. Fluid Mech.* 151,167–188.
- [6] Cazacu, O., Ionescu, I.R., Perrot,T., 2004. Penetration of a rigid body into a compressible rigid-viscoplastic fluid, In: ECCOMAS Proceedings, P. Neittaanmaki, T. Rossi, K. Majava, and O. Pironneau (eds.) W. Rodi and P. Le Qur (assoc. eds.),1–18.

- [7] Cazacu, O., Ionescu, I.R., Perrot,T., 2005. Steady-state flow of compressible rigid-viscoplastic media, submitted to Int. J. Engng. Sci.
- [8] Cristescu, N.D., Cazacu,O., Cristescu, C., 2002. A Model for Landslides. Canadian Geotechnical Journal 39,924-937.
- [9] Cristescu, N.D., Hunsche,U.,1998. Time Effects in Rock Mechanics, John Wiley & Sons.
- [10] Cristescu, N.,1967. Dynamic Plasticity, North Holland.
- [11] de Borst,R. and Groen,A.E.,2000. Computational strategies for standard soil plasticity models. In: Modelling in Geomechanics, Eds: M. Zaman, G. Gioda, J. Booker, John Wiley & Sons, LTD,24–50.
- [12] DiPerna, R.J., Lions, P.-L., 1989. Ordinary differential equations, Sobolev spaces and transport theory. Invent. Math. 98, 511–547.
- [13] Duvaut, G., Lions, J.-L., 1976. Inqualities in Mechanics and Physics, Springer Verlag.
- [14] Elaskar, S.A., Godoy, L.A., 1998. Constitutive relations for compressible granular materials using non-newtonian fluid mechanics. Int. J. Mech. Sci. 40, 1001–1081.
- [15] Goodman, M., Cowin, S., 1971. Two problems in the gravity flow of granular materials. J. Fluid Mech.45, 321–339.
- [16] Gray, D., Stiles,J., Celik,I. *Theoretical and Numerical studies of constitutive relations for frictional granular flow*, Final Report, U.S. Dept. of Energy.
- [17] Holmquist, T.J. , Johnson, G.R., Cook, W.H., 1993. A computational costitutive model for concrete subjected to large strains, high stain rates, and high pressures, 14th Int. Symp. on Ballistics, Quebec-City, Canada.
- [18] Ionescu, I.R., Sofonea, M., 1993. Functional and numerical methods in viscoplasticity, Oxford University Press.
- [19] Jenkins, J.T., Askari, E., 1991. Boundary conditions for rapid granular flows-phase interfaces. J. Fluid Mech., 223, 497–508.
- [20] Katona, M.G., 1984. Evaluation of viscoplastic cap model. J. of Geotech. Engrg. ASCE, 110(8), 1106–1125.
- [21] Lions, P.-L., 1996. Mathematical Topics in Fluid Mechanics, Oxford University Press.

- [22] Lemaitre, J., Chaboche, J.-L., 1990. Mechanics of Solid Materials, Cambridge University Press.
- [23] Malvern, L.E., Jenkins, D.A., 1990. Dynamic testing of laterally confined concrete, Technical Report ESL-TR-89-47, Air Force Engineering and Services Center.
- [24] Niandou, H., 1994. Etude du comportement rheologique et modélisation de l'argile de Tournemire. Applications à la stabilité des ouvrages, Ph.D. Thesis, University of Lille.
- [25] Nouri, A., Poupaud, F., 1995. An existence theorem for the multifluid Navier-Stokes problem. *J. Diff. Eq.*, 122 (1), 71–88.
- [26] Osborn, J., 1981. Loading on penetrators in concrete slabs, Report AFATL-TR-82-9 to the Air Force Armament Laboratory.
- [27] Perzyna, P., 1966, Fundamental problems in viscoplasticity, *Adv. Appl. Mech.*, 9, 243–377.
- [28] Prager, W. and Hodge, P., 1968. *Theory of Perfectly Plastic Solids*, Dover, New York.
- [29] Roscoe, K. H., Burland, J. B., 1968. On the generalized behavior of wet clay. *Engineering Plasticity* 48, 535–609.
- [30] Ross, C.A., Jerome, D.M., Tedesco, J.W. Hughes, M.L., 1996. Moisture and strain rate effects in concrete. *ACI Materials Journal* 93(3), 293–300.
- [31] Savage, S., 1979. Gravity flow of cohesionless granular materials in chutes and channels, *J. Fluid Mech.* 92, 53–63.
- [32] Schmidt, M.J., Cazacu, O., Ross, C.A., Cristescu, N.D., 2001. Dynamic behavior of mortar: experimental data and modeling, *Proceedings of the 10th International Conference on Computer Methods and Advances in Geomechanics*, Tucson, Arizona.
- [33] Vinay, G., Wachs, A., Agassant, J.-F., 2005. Numerical simulation of non-isothermal viscoplastic waxy crude oil flows, *J. Non-Newtonian Fluid Mech.* 128, 144–162.
- [34] Vulliet, L., 2000. Natural slopes in slow movement. In: Modelling in Geomechanics, Eds: M. Zaman, G. Gioda, J. Booker, John Wiley & Sons, LTD, 653–674.

3 Task 2: Numerical modeling of projectile penetration into compressible rigid visco-plastic media

3.1 Introduction

One of the many challenges associated with modeling penetration is that very limited experimental data are available. Although progress has been made in instrumentation and diagnostic techniques that allow accurate measurements of impact velocity and projectile deceleration, in-target instrumentation is limited. Thus, information concerning the stress-time response in the target during penetration is lacking (see for example, Gran and Frew [1]). To gain insights and fundamental understanding of the phenomena involved, numerical simulations of penetration processes play a key role.

For modeling the deformation of the target during penetration Lagrangian and Eulerian methods have been used (see for e.g. the survey by Hertel [2]). Each of these methods has advantages and disadvantages as a tool to model penetration. With Lagrangian methods, the conservation equations are solved using either finite difference or finite element techniques on a mesh which moves with the material. The material interfaces are tracked in a sharp fashion. However, severe deformation leads to mesh tangling or distortion, hence considerable complexity is enjoined by the need for remeshing. Mesh-less methods (e.g. [3]-[6]) or a combination of finite element methods with embedded boundary tracking and local enrichment (e.g.[7]) have emerged in recent years. When using Eulerian methods, the conservation equations are solved using either finite difference or finite volume techniques. However, when using such methods the main challenge is to be able to track moving material boundaries (i.e. problems related to recognition of material interfaces or surfaces). Such difficulties are the driving force for the development of Arbitrary Lagrangian Eulerian(ALE) and level set methods (see for e.g. [2, 8]).

It is to be noted that the material models used in conjunction with the aforementioned methods apply mainly to penetration into metallic materials. It was shown (see for instance [9, 10]) that the use of an Eulerian setting and of a fluid-type constitutive equations presents clear advantages over other methods employed for modeling penetration in metallic materials. However, implicit in these fluid-type models is the hypothesis of incompressibility, thus these models cannot describe the irreversible volumetric changes observed in geologic or cementitious materials. Indeed, from post-test observations of the density distribution in the target it can be clearly seen that when subjected to dynamic loading, porous and particulate materials show large irreversible volumetric and shear deformations, the behavior being highly sensitive to the strain rate (e.g. [11, 12, 13]). Batra and Gobinath [14] have proposed a compressible model that accounts for the rate dependence of the shear response. Hardening effects are neglected and the pressure-density response is

given by a gas type state equation which cannot capture plastic volumetric effects. Recently, for modeling penetration in concrete, a purely hydrodynamic treatment was used in [15] while LS-DYNA finite-element simulations have been reported by [16]. Under this grant support, computational techniques for modeling steady-state flow of a compressible rigid viscoplastic fluid have been developed. Illustration of the application of these methods was provided for cementitious materials considered to obey a revisited Bingham type model [18], which accounts for plastic volumetric deformations. The reader is referred to the journal paper Cazacu et al [17] in which this work is presented in detail.

In the following we will present the computational methods developed for modeling non-steady penetration of a rigid projectile into cementitious targets. To capture the solid-fluid transition in behavior at high strain rates observed in such media and account for damage/plasticity couplings and how these dissipative mechanisms are influenced by the strain rate, we consider a compressible rigid viscoplastic fluid model, that we called Bingham revisited (see section 2.4.2 of this report and the journal paper in which we published the model [18]).

A hybrid time-discretization is used to model the non-stationary flow of the target material and the projectile-target interaction, i.e. an explicit Euler method for the projectile equation and a forward (implicit) method for the target boundary value problem. At each time step, a mixed finite-element and finite-volume strategy is used to solve the boundary value problem in the target. Specifically, algorithms for solving the nonlinear variational problem involving the velocity field via the finite element approximation are developed while finite-volume techniques are adopted for solving the hyperbolic mass conservation and damage evolution equation.

It is to be noted that when using a rigid compressible viscoplastic fluid equation, additional difficulties arise due to the non-smoothness of the plastic terms. Moreover, since in the constitutive description for the target material a rigid unloading hypothesis is considered, the variational inequality to be solved has unilateral constraints for the velocity divergence. Thus, we cannot simply make use of finite element techniques developed for Navier-Stokes fluids. Therefore, to solve the velocity problem, a decomposition-coordination formulation coupled with the augmented lagrangian method, developed by [19, 20] (for a comprehensive review see also [21]) for the Bingham fluid is adapted here. The velocity problem and the methods used to solve it are similar to those developed in [17] for modeling steady-state flow of a revisited Bingham fluid.

It is shown that using the material model and algorithms presented in this paper, it is possible to provide details concerning the stress and kinematic fields in the target. Specifically, the density changes around the penetration tunnel, the shape and location of the rigid/plastic boundary, the extent of damage due to air void collapse in such materials are accurately predicted. Moreover, the numerical model is robust and computationally inexpensive. This is due to the fact that in modeling penetration using a rigid-type model only a small zone around the projectile is deformed and thus we can restrict the computations to a small bounded domain

around the projectile. Another advantage of using a fluid-type approach is that the computations are done in a fixed domain and there is no need to mesh different domains at each time interval.

One of the many challenges associated with simulating penetration in cementitious materials is related to the lack of experimental data for the high pressures and high strain rates involved (see e.g.[22]. To assess the effects of the constants involved in the material model that cannot be determined explicitly from experimental data, a parametric study was also performed. Thus, we analyzed the sensitivity of the penetration depth calculations with respect to shear and volumetric viscosities, cut-off yield limit, and frictional constants. The results of this study provides insights into the relative importance of the plastic and viscous effects on the penetration process.

3.2 Constitutive model for the target material

In this section, we give an overview of the material model used for the target. To capture the solid-fluid transition in behavior at high strain rates observed in cementitious porous media, account for damage/plasticity couplings and how these dissipative mechanisms are influenced by the strain rate we consider a compressible rigid viscoplastic fluid constitutive equation. The general form, proposed in [18](see also section 4 of the present document) is:

$$\mathbf{D}(\mathbf{v}) \in \mathcal{C}, \begin{cases} \boldsymbol{\sigma} = \alpha(\mathbf{D}(\mathbf{v}), \mathbf{h})\mathbf{I} + \beta(\mathbf{D}(\mathbf{v}), \mathbf{h})\mathbf{D}'(\mathbf{v}) & \text{if } |\mathbf{D}(\mathbf{v})| \neq 0, \\ F(\boldsymbol{\sigma}, \mathbf{h}) \leq 0 & \text{if } |\mathbf{D}(\mathbf{v})| = 0, \end{cases} \quad (65)$$

In (65), $\boldsymbol{\sigma}$ denotes the Cauchy stress tensor, \mathbf{D} is the rate of deformation tensor, $\mathbf{D} = \mathbf{D}(\mathbf{v}) = (\nabla \mathbf{v} + \nabla^T \mathbf{v})/2$ (\mathbf{v} denotes the velocity field) while $\mathbf{D}' = \mathbf{D} - \text{tr}(\mathbf{D})/3\mathbf{I}$ is its deviator, \mathbf{I} is the identity tensor, $\mathbf{h} \in \mathbb{R}^n$ is the vector of n scalar internal variables. $F(\boldsymbol{\sigma}, \mathbf{h})$ is the yield function and $\mathcal{C} \subset \mathbb{R}_S^{3 \times 3}$ represents a set of kinematic constraints, while α and β are scalar functions of their arguments. The invariance under superposed rigid body motions requires that α and β are isotropic functions of \mathbf{D} .

The presentation of the model (65) is completed by providing the evolution equations for the internal variables \mathbf{h} . It is assumed that the total (particular) derivative of \mathbf{h} is a function of \mathbf{h} and the stretch tensor \mathbf{D} , i.e.

$$\frac{d\mathbf{h}}{dt} = \frac{\partial \mathbf{h}}{\partial t} + \mathbf{v} \cdot \nabla \mathbf{h} = \mathbf{H}(\mathbf{D}, \mathbf{h}). \quad (66)$$

If there is flow (i.e. in the visco-plastic regime where $\mathbf{D} \neq 0$), then $F(\alpha(\mathbf{D}, \mathbf{h})\mathbf{I} + \beta(\mathbf{D}, \mathbf{h})\mathbf{D}', \mathbf{h}) > 0$, for all $\mathbf{D} \in \mathcal{C} \setminus \{0\}$. It should be noted that at difference with a classic fluid constitutive equation, for a rigid viscoplastic material the constitutive functions α and β are not defined and cannot be prolonged by continuity in $\mathbf{D} = 0$. To ensure continuous transition between flow and no-flow states, it is required that

$\alpha(\cdot, \mathbf{h})$, $\beta(\cdot, \mathbf{h})$ are continuous on $\mathcal{C} \setminus 0$. The continuity of the transition between flow and no flow reads: $F(\alpha(\mathbf{D}, \mathbf{h})\mathbf{I} + \beta(\mathbf{D}, \mathbf{h})\mathbf{D}', \mathbf{h}) \rightarrow 0$, for $\mathbf{D} \rightarrow 0$ with $\mathbf{D} \in \mathcal{C} \setminus 0$, while the fact that the dissipated power has to be nonnegative leads to $\boldsymbol{\sigma} : \mathbf{D} = \alpha(\mathbf{D}, \mathbf{h})\text{tr}(\mathbf{D}) + \beta(\mathbf{D}, \mathbf{h})|\mathbf{D}'|^2 \geq 0$ for all $\mathbf{D} \in \mathcal{C}$.

Two general procedures for determining the expressions of the constitutive functions F , α , and β such that the model (65)-(66) is consistent (i.e. the above compatibility conditions are satisfied) are provided in [18]. Although all the numerical methods and techniques developed in this paper are valid for the constitutive equation (65)-(66) in its general form, in this paper we consider a specific compressible rigid viscoplastic model. In this model it is assumed that yielding under deviatoric conditions is of Von Mises type with yield limit κ depending on two internal variables: the current density ρ and the damage parameter δ , i.e. $n = 2$, $\mathbf{h} = (\rho; \delta)$. Thus, the effect of the density on flow is taken into account while the damage parameter is associated to the loss of cohesive strength due to air pore collapse.

For hydrostatic conditions, the response is described by a pressure-density relationship of the form: $p = p_c(\rho)$. Note that a full equation of state which gives a complete thermo-dynamical characterization is not available for porous cementitious materials (see for example the very recent survey and experimental study on concrete [22]). This is due to the fact that using the current testing methods (detonation and flyer-impact testing) only data pairs of pressure-density points can be obtained.

Data available for cementitious materials (see for instance [23]) indicate a stiff response upon unloading. Thus, the reversible decrease of volume can be neglected and the unloading process can be considered rigid (the density acquired at the end of the loading process is preserved during unloading). Hence, the yield condition is of the form:

$$F(p, q, \rho, \delta) = \sqrt{\left[\sqrt{\frac{2}{3}}q - \kappa(\rho, \delta)\right]_+^2 + [p + p_c(\rho)]_-^2}. \quad (67)$$

where $[x]_+ = (|x| + x)/2$, $[x]_- = (|x| - x)/2$ and $p = \frac{\text{tr}(\boldsymbol{\sigma})}{3}$, $q = \sqrt{\frac{3}{2}}|\boldsymbol{\sigma}'|$. Using this yield function and the superposition technique (i.e. compressible Navier-Stokes fluid superposed on an associated plastic solid described by (67)) we can deduce, (see [18]), the following constitutive equation called the revisited Bingham fluid model. The deviatoric part of this model is:

$$\begin{cases} \boldsymbol{\sigma}' = \left[2\eta(\rho) + \frac{\kappa(\rho, \delta)}{|\mathbf{D}'|}\right]\mathbf{D}' & \text{if } |\mathbf{D}'| \neq 0 \\ |\boldsymbol{\sigma}'| \leq \kappa(\rho, \delta) & \text{if } |\mathbf{D}'| = 0, \end{cases} \quad (68)$$

while its spherical part is:

$$\text{div}(\mathbf{v}) \leq 0, \quad \begin{cases} \text{tr}(\boldsymbol{\sigma})/3 = -p_c(\rho) + [\lambda(\rho) + 2\eta(\rho)/3]\text{div}(\mathbf{v}) & \text{if } \text{div}(\mathbf{v}) < 0 \\ \text{tr}(\boldsymbol{\sigma})/3 \geq -p_c(\rho) & \text{if } \text{div}(\mathbf{v}) = 0. \end{cases} \quad (69)$$

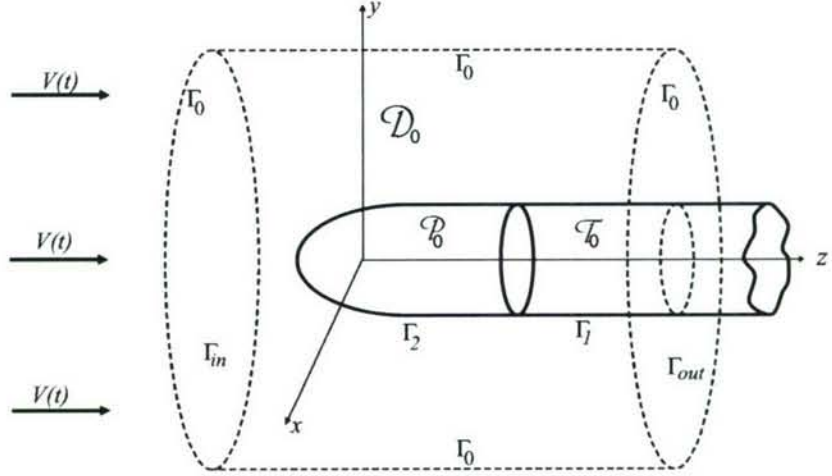


Figure 8: Representation of the domain \mathcal{D}_0 for the tunnelling stage of penetration.

Note that the classical Bingham fluid is recovered if in (68) the incompressibility condition (i.e. $\operatorname{div} \mathbf{v} = 0$) is imposed.

The kinematic restriction is $\mathcal{C} = \{\mathbf{D} ; \operatorname{tr}(\mathbf{D}) \leq 0\}$ i.e. the flow is compressible and unloading is rigid. In many solid-type models, p_c and κ are expressed as functions of the compaction level (or volumetric strain) $\mu = \rho/\rho_0 - 1$ instead of the density ρ (here ρ_0 is the initial density prior to loading). Note that (68)-(69) can be recast in the form that is generally used in hydrocode calculations by eliminating μ between $\kappa = \kappa(\mu, \delta)$ and $p_c = p_c(\mu)$.

3.3 Geometry and fields equations

When a penetrator impacts a semi-infinite geological, or cementitious target the material is displaced radially and as a result a tunnel-shaped crater is formed in the target. The entrance portion of the crater is generally produced by spallation in the vicinity of the impact site. The crater entrance is typically wide and shallow, but it rapidly evolves into a circular tunnel.

Our objective is to model the tunnelling phase of the penetration, when the full length of the projectile is in the target and the target material flows around the projectile. It is assumed that the projectile is rigid.

Let us denote by \mathcal{P}_0 and \mathcal{T}_0 the domains occupied by the projectile and by the semi-infinite tunnel in the coordinates $Oxyz$ which are linked to the projectile (see Figure 1).

Let $Ox_1x_2x_3$ be the coordinates attached to the target and let $-V(t)\mathbf{e}_3$ be the velocity of the projectile at the moment $t \geq 0$. The two system of coordinates

coincide at $t = 0$ and we have

$$x_1 = x, \quad x_2 = y, \quad x_3 = z - \int_0^t V(s) \, ds.$$

The target occupies the variable domain \mathcal{D}_t which is the whole space \mathbb{R}^3 without the projectile $\mathcal{P}_t = \{(x_1, x_2, x_3); (x_1, x_2, x_3 + \int_0^t V(s) \, ds) \in \mathcal{P}_0\}$ and the infinite tunnel $\mathcal{T}_t = \{(x_1, x_2, x_3); (x_1, x_2, x_3 + \int_0^t V(s) \, ds) \in \mathcal{T}_0\}$ behind it, i.e. $\mathcal{D}_t = \mathbb{R}^3 \setminus (\mathcal{P}_t \cup \mathcal{T}_t)$, and it corresponds to $\mathcal{D}_0 = \mathbb{R}^3 \setminus (\mathcal{P}_0 \cup \mathcal{T}_0)$ in the coordinates linked to the projectile. We denote by Γ_1^t, Γ_2^t the part of the boundaries of \mathcal{T}_t and \mathcal{P}_t which are in contact with the target, i.e. $\partial\mathcal{D}_t = \Gamma_1^t \cup \Gamma_2^t$, which corresponds to $\partial\mathcal{D}_0 = \Gamma_1 \cup \Gamma_2$, in $Oxyz$ coordinates.

Next, we present the equations governing the non stationary flow of a rigid viscoplastic material described by the constitutive equations (67) and (68)-(69). In order to write the conservation laws in the fixed domain \mathcal{D}_0 instead of the variable domain \mathcal{D}_t , we denote by $\mathbf{v} : [0, T] \times \mathcal{D}_0 \rightarrow \mathbb{R}^3$ the relative velocity field given by

$$\mathbf{v}(t, x, y, z) = \mathbf{v}(t, x_1, x_2, x_3) + V(t)\mathbf{e}_z,$$

where \mathbf{v} is the Eulerian velocity field in \mathcal{D}_t . The other fields, i.e. the stress $\boldsymbol{\sigma}$, density ρ and damage δ will have the same notations in both systems of coordinates.

The momentum balance law in the Eulerian coordinates $Oxyz$ reads

$$\rho(t)[\partial_t \mathbf{v}(t) + (\mathbf{v}(t) \cdot \nabla) \mathbf{v}(t) - \dot{V}(t)\mathbf{e}_z] - \operatorname{div} \boldsymbol{\sigma}(t) = 0 \quad \text{in } \mathcal{D}_0, \quad (70)$$

the continuity equation is

$$\frac{\partial \rho}{\partial t} + \mathbf{v} \cdot \nabla \rho = -\rho \operatorname{div}(\mathbf{v}), \quad \text{in } \mathcal{D}_0, \quad (71)$$

while the damage evolution law can be written as

$$\frac{\partial \delta}{\partial t} + \mathbf{v} \cdot \nabla \delta = H(\rho, \delta, \mathbf{D}(\mathbf{v})) \quad \text{in } \mathcal{D}_0. \quad (72)$$

The conditions at infinity for the target in the coordinates linked to the projectile read:

$$\mathbf{v}(t, x, y, z) = V(t)\mathbf{e}_z \quad \text{for } ||(x, y, z)|| \rightarrow +\infty, \quad (73)$$

$$\rho(t, x, y, z) = \rho^0, \quad \delta(t, x, y, z) = 0 \quad \text{for } z \rightarrow -\infty. \quad (74)$$

The mechanical model considered for the target material is rigid-viscoplastic. Thus, with the exception of a domain around the projectile where viscoplastic deformations occur, the target material is in rigid motion. Hence, the domain \mathcal{D}_0 , affected by the impact event, can be restricted from the whole space to a bounded

region (depicted in Figure 1 with interrupted lines). To enable reasonable computational effort and yet ensure that we capture the viscoplastic region in its entirety (i.e. the boundary conditions at infinity are accurately described), we limit the extent of this domain to 5 projectile radii. This assumption appears to be supported by experimental evidence. Indeed, post-test observations indicate that the tunnel is of the order of the projectile diameter. For both grout and concrete targets a change in density in the region around the penetration tunnel radially outward from the edge of the tunnel to a distance of 1 – 1.5 projectile diameters was reported (see Jones et al [24]).

Using this assumption the boundary conditions at infinity (73)-(74) are replaced by

$$\mathbf{v}(t) = V(t)\mathbf{e}_z \text{ on } \Gamma_0, \quad \rho(t) = \rho^0, \delta(t) = 0 \text{ on } \Gamma_{in}. \quad (75)$$

On the surface in contact with the tunnel, Γ_1 , the stress vector vanishes

$$\boldsymbol{\sigma}(t, x)\mathbf{n} = 0, \quad (76)$$

where \mathbf{n} stands for the outward unit normal on $\partial\mathcal{D}_0$, while frictional contact is assumed on the boundary of the projectile Γ_2 .

The mechanics of friction at high speed of sliding is very complex. Much of the work reported in the literature is at lower speeds or pressures than those occurring during a penetration event. In view of this, in our analysis we assume that a Coulomb friction law applies. However, in order to capture the rate effect on the frictional contact between the concrete target and the metallic penetrator, a slip rate dependent friction coefficient is assumed, i.e.:

$$u_n = 0, \quad \begin{cases} \mathbf{v}_t = 0 \implies |\boldsymbol{\sigma}_t| \leq \mathcal{F}|\sigma_n|, \\ \mathbf{v}_t \neq 0 \implies \boldsymbol{\sigma}_t = -\mathcal{F}|\sigma_n| \frac{\mathbf{v}_t}{|\mathbf{v}_t|}, \end{cases} \quad (77)$$

where $u_n = \mathbf{v} \cdot \mathbf{n}$ is normal velocity, $\sigma_n = \boldsymbol{\sigma} \mathbf{n} \cdot \mathbf{n}$ is the normal stress, $\mathbf{v}_t = \mathbf{v} - u_n \mathbf{n}$ is the tangential velocity, $\boldsymbol{\sigma}_t = \boldsymbol{\sigma} - (\boldsymbol{\sigma} \cdot \mathbf{n})\mathbf{n}$ stands for the tangential stress and \mathcal{F} is the friction coefficient. According to (77), the tangential (friction) stress is bounded by the normal stress multiplied by the friction coefficient \mathcal{F} . If such a limit is not attained sliding cannot occur; otherwise the friction stress is opposite to the slip rate. The friction coefficient will also be considered variable. Experimental observations indicate that the friction coefficient depends on the slip rate $|\mathbf{v}_t|$ i.e. $\mathcal{F} = \mathcal{F}(|\mathbf{v}_t|)$. The simplest law of variation of \mathcal{F} on the slip rate is a discontinuous jump from a “static” value (for $|\mathbf{v}_t| = 0$) down to a “dynamic” or “kinetic” value (for $|\mathbf{v}_t| \neq 0$). In this work, we will consider a smooth and decreasing function $\mathcal{F} = \mathcal{F}(|\mathbf{v}_t|)$ of the slip rate.

If we denote by M the mass of the projectile then the fluid structure interaction equation is

$$M\dot{\mathbf{V}}(t) = - \int_{\Gamma_2} \boldsymbol{\sigma}(t)\mathbf{n} \cdot \mathbf{e}_z. \quad (78)$$

Finally, the initial conditions are

$$\mathbf{v}(0) = \mathbf{v}_0, \quad \rho(0) = \rho_0, \quad \delta(0) = \delta_0, \quad V(0) = V_0 \quad (79)$$

where \mathbf{v}_0, ρ_0 , and δ_0 are the initial relative velocity, density, and damage, respectively. We suppose that the initial fields are smooth and compatible with the boundary conditions, i.e. no discontinuities are generated initially.

3.4 The algorithm

3.4.1 Time discretization

Let Δt be the time step and let us denote by $\mathbf{v}^k, \boldsymbol{\sigma}^k, \rho^k, \delta^k, V^k$ the values of $\mathbf{v}(k\Delta t), \boldsymbol{\sigma}(k\Delta t), \rho(k\Delta t), \delta(k\Delta t)$ and $V(k\Delta t)$. Suppose that we have computed all these values at $t = k\Delta t$. The time explicit (forward) Euler scheme for the projectile equation (78) will then provide V^{k+1}

$$V^{k+1} = V^k - \frac{\Delta t}{M} \int_{\Gamma_0^2} \boldsymbol{\sigma}^k \mathbf{n} \cdot \mathbf{e}_z. \quad (80)$$

and the time implicit (backward) Euler scheme for (70)- (72) gives the following nonlinear equations for $\mathbf{v}^{k+1}, \boldsymbol{\sigma}^{k+1}, \rho^{k+1}$ and δ^{k+1}

$$\rho^{k+1}[\mathbf{v}^{k+1} + \Delta t \mathbf{v}^{k+1} \cdot \nabla \mathbf{v}^{k+1}] - \Delta t \operatorname{div} \boldsymbol{\sigma}^{k+1} = \rho^{k+1} \mathbf{f}_k \quad \text{in } \mathcal{D}_0, \quad (81)$$

$$\rho^{k+1} + \Delta t \operatorname{div}(\rho^{k+1} \mathbf{v}^{k+1}) = \rho^k \quad \text{in } \mathcal{D}_0, \quad (82)$$

$$\delta^{k+1} + \Delta t \nabla \delta^{k+1} \cdot \mathbf{v}^{k+1} = \delta^k + \Delta t H(\rho^{k+1}, \delta^{k+1}, \mathbf{D}(\mathbf{v}^{k+1})) \quad \text{in } \mathcal{D}_0. \quad (83)$$

where $\mathbf{f}_k = \mathbf{v}^k + (V^{k+1} - V^k) \mathbf{e}_z$. To this set of equations, we have to add the constitutive equations (67),(68)-(69) which link all three unknowns i.e. $\mathbf{v}^{k+1}, \boldsymbol{\sigma}^{k+1}, \rho^{k+1}$. The conditions at the "artificial" boundary of \mathcal{D}_0 , which replace the conditions at infinity, are

$$\mathbf{v}^{k+1} = V^{k+1} \mathbf{e}_z \quad \text{on } \Gamma_0, \quad \rho^{k+1} = \rho^0, \quad \delta^{k+1} = 0, \quad \text{on } \Gamma_{in}. \quad (84)$$

Moreover, $u_n^{k+1}, \mathbf{v}_\tau^{k+1}, \sigma_n^{k+1}$ and $\boldsymbol{\sigma}_\tau^{k+1}$ have to satisfy the friction law (77).

Setting

$$\mathcal{W}^{k+1} = \{\mathbf{v} \in H^1(\mathcal{D}_0)^3 ; \mathbf{v} = V^{k+1} \mathbf{e}_z \text{ on } \Gamma_0, v_n = 0 \text{ on } \Gamma_2\},$$

the kinematic admissible set is:

$$\mathcal{V}^{k+1} = \{\mathbf{v} \in \mathcal{W}^{k+1} ; \operatorname{div} \mathbf{v} \leq 0 \text{ in } \mathcal{D}_0\},$$

and the variational formulation for the velocity field $\mathbf{v}^{k+1} \in \mathcal{V}^{k+1}$ is:

$$\int_{\mathcal{D}_0} \rho^{k+1} \mathbf{v}^{k+1} \cdot (\mathbf{v} - \mathbf{v}^{k+1}) + \Delta t \left\{ \int_{\mathcal{D}_0} \rho^{k+1} \mathbf{v}^{k+1} \cdot \nabla \mathbf{v}^{k+1} \cdot (\mathbf{v} - \mathbf{v}^{k+1}) + \right.$$

$$\begin{aligned}
& \int_{\mathcal{D}_0} 2\eta(\rho^{k+1}) D'(\mathbf{v}^{k+1}) : (D'(\mathbf{v}) - D'(\mathbf{v}^{k+1})) + \int_{\mathcal{D}_0} \kappa(\rho^{k+1}, \delta^{k+1}) (|D'(\mathbf{v})| - |D'(\mathbf{v}^{k+1})|) \\
& + \int_{\mathcal{D}_0} [(\lambda(\rho^{k+1}) + \frac{2}{3}\eta(\rho^{k+1})) \operatorname{div} \mathbf{v}^{k+1} - p_c(\rho^{k+1})] \operatorname{div}(\mathbf{v} - \mathbf{v}^{k+1}) \\
& + \int_{\Gamma_2} \mathcal{F}(|\mathbf{v}_\tau^{k+1}|) |\sigma_n^{k+1}| (|\mathbf{v}_\tau| - |\mathbf{v}_\tau^{k+1}|) \} \geq \int_{\mathcal{D}_0} \rho^{k+1} \mathbf{f}_k \cdot (\mathbf{v} - \mathbf{v}^{k+1}),
\end{aligned} \tag{85}$$

for all $\mathbf{v} \in \mathcal{V}^{k+1}$.

3.4.2 The general scheme

Let us fix the iteration in time k . The numerical algorithm for solving the nonlinear equations (81)-(83), consists of solving alternatively the variational inequality (85) for the velocity field and the equations (82)-(83) for the density and damage fields. More precisely, we will distinguish two problems : the "velocity problem" and the "density/damage problem".

For the velocity problem (at iteration n of the algorithm), we assume that $\rho^{k+1} = \rho^{k+1,n}$ and $\delta^{k+1} = \delta^{k+1,n}$ are given, i.e. the distributions of $p = p_c(\rho^{k+1})$, $\eta = \eta(\rho^{k+1})$, $\lambda = \lambda(\rho^{k+1})$ and $\kappa = \kappa(\rho^{k+1}, \delta^{k+1})$ are known, and we find the velocity $\mathbf{v}^{k+1} = \mathbf{v}^{k+1,n+1} \in \mathcal{V}$ by solving the variational inequality (85).

The density/damage problem (at iteration n of the algorithm) consists in finding the density and damage fields i.e. $\rho^{k+1} = \rho^{k+1,n+1}$ and $\delta^{k+1} = \delta^{k+1,n+1}$ solutions of (82) and

$$\delta^{k+1} + \Delta t \operatorname{div}(\delta^{k+1} \mathbf{v}^{k+1}) = H^{k,n} \quad \text{in } \mathcal{D}_0, \tag{86}$$

where $H^{k,n} = \delta^k + \Delta t [H(\rho^{k+1,n}, \delta^{k+1,n}, \mathbf{D}(\mathbf{v}^{k+1})) + \delta^{k+1,n} \operatorname{div} \mathbf{v}^{k+1}]$, assuming that $\mathbf{v}^{k+1} = \mathbf{v}^{k+1,n+1}$ is known.

Since we will suppose that the time iteration is fixed, in the following we will omit the subscript $k+1$. Moreover, in order to simplify the notations, we will also omit the subscript $n+1$.

3.4.3 The velocity problem

It is to be noted that in the case of a rigid compressible viscoplastic fluid, additional difficulties arise from the non differentiability of the plastic terms and from the unilateral constraints on the velocity divergence. That means that we cannot simply make use of the finite element techniques developed for Navier-Stokes fluids (see for instance [25, 26]). To solve the velocity problem, a decomposition-coordination formulation coupled with the augmented lagrangian method (see [19, 20]) will be adapted for the material model considered (67),(68)-(69). After time discretization, the variational formulation in terms of velocities is similar to that corresponding to the stationary flow of a revisited Bingham fluid given in [17]. Although the numerical techniques developed here for the velocity problem are very close to that

proposed in [17], in the following we present its main features and refer the reader to [17] for further details.

\mathcal{D}_0 is discretized by using a family of triangulations $(\mathcal{T}_h)_h$ made of finite elements (of degree 2), where $h > 0$ is the discretization parameter representing the greatest diameter of a triangle in \mathcal{T}_h . The finite element space \mathcal{W}_h , which is an internal approximation of \mathcal{W} will be denoted by W_h , while $\mathcal{V}_h = \mathcal{V} \cap \mathcal{W}_h$. Then, the velocity problem is discretized by considering $\mathbf{v}_h \in \mathcal{V}_h$ which satisfies the variational inequality (85) for all $\mathbf{v} \in \mathcal{V}_h$. In order to simplify the notations, we shall omit throughout this subsection the index h .

For all $\mathbf{w} \in \mathcal{V}_h$ we define $J_{\mathbf{w}} : V_h \rightarrow \mathbb{R}$ as

$$\begin{aligned} J_{\mathbf{w}}(\mathbf{v}) = & \int_{\mathcal{D}_0} \frac{\rho}{2} |\mathbf{v}|^2 + \Delta t \left\{ \int_{\mathcal{D}_0} \eta |\mathbf{D}'(\mathbf{v})|^2 + \int_{\mathcal{D}_0} \left(\frac{\lambda}{2} + \frac{\eta}{3} \right) (\operatorname{div} \mathbf{v})^2 + \int_{\mathcal{D}_0} \kappa |\mathbf{D}'(\mathbf{v})| + \right. \\ & \left. \int_{\Gamma_2} \mathcal{F}(|\mathbf{w}_t|) |\sigma_n(\mathbf{w})| |\mathbf{v}_t| + \int_{\mathcal{D}} \rho (\mathbf{w} \cdot \nabla) \mathbf{w} \cdot \mathbf{v} - \int_{\mathcal{D}_0} p \operatorname{div} \mathbf{v} \right\} - \int_{\mathcal{D}_0} \rho \mathbf{f} \cdot \mathbf{v}. \end{aligned} \quad (87)$$

and rewrite the velocity problem as a quasi-variational problem

$$\mathbf{v} \in \mathcal{V}_h, \quad J_{\mathbf{v}}(\mathbf{v}) = \min_{\mathbf{v} \in \mathcal{V}_h} J_{\mathbf{v}}(\mathbf{v}). \quad (88)$$

To reduce the quasi-variational problem to a sequence of minimization problems, we use the following iterative algorithm (*IA*) : given $\mathbf{v}^{j-1} \in \mathcal{V}_h$ find $\mathbf{v}^j \in \mathcal{V}_h$, the solution of the following minimization problem for $J_j(\mathbf{v}) = J_{\mathbf{v}^{j-1}}(\mathbf{v})$

$$\mathbf{v}^j \in \mathcal{V}_h, \quad J_j(\mathbf{v}^j) = \min_{\mathbf{v} \in \mathcal{V}_h} J_j(\mathbf{v}). \quad (89)$$

Since J_j is not Gâteaux differentiable, one can use a regularization technique (see for instance [27, 28]). With this technique, the material is not completely rigid anymore, and so it is difficult to capture accurately the shape of the rigid zone. To overcome this difficulty and describe the rigid/viscoplastic boundary sharply, we adapt the decomposition-coordination formulation coupled with the augmented lagrangian method originally introduced for the incompressible Bingham fluid in [19, 20]. On the other hand, for the frictional terms, which are also non-differentiable, we shall use a classical regularization technique because in the applications considered (penetration into geological materials) the slip rate is always non-zero.

Let us consider the spaces of lagrangian multipliers: Δ_h , which denote tensor valued polynomial functions of degree one on each triangle, and Θ_h which denote real valued polynomial functions of degree one, respectively. The augmented lagrangian

$\mathcal{L}_j : V_h \times \Delta_h \times \Theta_h \times \Delta_h \rightarrow \mathbb{R}$ is :

$$\begin{aligned}
\mathcal{L}_j(\mathbf{v}, \boldsymbol{\sigma}, \theta, \boldsymbol{\gamma}) = & \int_{\mathcal{D}_0} \frac{\rho}{2} |\mathbf{v}|^2 + \Delta t \left\{ \int_{\mathcal{D}_0} \eta |\boldsymbol{\gamma}|^2 + \int_{\mathcal{D}_0} \left(\frac{\lambda}{2} + \frac{\eta}{3} \right) \theta^2 + \int_{\mathcal{D}_0} \kappa |\boldsymbol{\gamma}| - \right. \\
& \int_{\mathcal{D}_0} p \theta + \int_{\Gamma_2} \mathcal{F}(|\mathbf{v}_t^{j-1}|) |\sigma_n(\mathbf{v}^{j-1})| \frac{\mathbf{v}_t^{j-1} \cdot \mathbf{v}_t}{\sqrt{|\mathbf{v}_t^{j-1}|^2 + \epsilon^2}} + \int_{\mathcal{D}_0} \rho (\mathbf{v}^{j-1} \cdot \nabla) \mathbf{v}^{j-1} \cdot \mathbf{v} + \\
& \left. \int_{\mathcal{D}_0} (\mathbf{D}'(\mathbf{v}) - \boldsymbol{\gamma}) : \boldsymbol{\sigma}' + \int_{\mathcal{D}_0} (\theta - \operatorname{div} \mathbf{v}) \operatorname{trace}(\boldsymbol{\sigma}) \right\} - \int_{\mathcal{D}_0} \rho \mathbf{f} \cdot \mathbf{v} + \\
& r_D \int_{\mathcal{D}_0} |\mathbf{D}'(\mathbf{v}) - \boldsymbol{\gamma}|^2 + r_H \int_{\mathcal{D}_0} |\theta - \operatorname{div} \mathbf{v}|^2. \tag{90}
\end{aligned}$$

where r_H and r_D are strictly positive constants. Here $\boldsymbol{\gamma} \in \Delta_h$ stands for $\mathbf{D}'(\mathbf{v})$, $\theta \in \Theta_h$ stands for $\operatorname{div} \mathbf{v}$, and $\boldsymbol{\sigma} \in \Delta_h$ is a lagrangian multiplier. Thus, the minimization problem (89) becomes: find $\mathbf{v}^j \in \mathcal{V}_h$, $\boldsymbol{\sigma}^j \in \Delta_h$, $\theta^j \in \Theta_h$ and $\boldsymbol{\gamma}^j \in \Delta_h$ such that

$$\sup_{\theta, \boldsymbol{\sigma}, \boldsymbol{\gamma}} \mathcal{L}_j(\mathbf{v}^j, \boldsymbol{\sigma}, \theta, \boldsymbol{\gamma}) \leq \mathcal{L}_j(\mathbf{v}^k, \boldsymbol{\sigma}^j, \theta^j, \boldsymbol{\gamma}^j) \leq \inf_{\mathbf{v} \in \mathcal{V}_h} \mathcal{L}_j(\mathbf{v}, \boldsymbol{\sigma}^j, \theta^j, \boldsymbol{\gamma}^j). \tag{91}$$

In order to solve the above saddle point problem, we use an Uzawa-type algorithm (UA). The interest in using this algorithm is that it transforms the non-differentiable problem into a sequence of completely standard computations.

Let first define the functions f_H and f_D , useful in the description of the algorithm:

$$\mathbf{f}_D(\boldsymbol{\sigma}, a) = \frac{1}{2\eta(\rho) + a} \left[1 - \frac{\kappa(\rho, \delta)}{|\boldsymbol{\sigma}'|} \right]_+ \boldsymbol{\sigma}', \quad f_H(\boldsymbol{\sigma}, a) = - \left[\frac{3p(\rho) + \operatorname{tr} \boldsymbol{\sigma}}{3\lambda(\rho) + 2\eta(\rho) + a} \right]_-, \tag{92}$$

where $[x]_+ = (x + |x|)/2$ and $[x]_- = (|x| - x)/2$ are the positive and the negative part of $[x]$, respectively. The (UA) algorithm, starts by choosing $\boldsymbol{\sigma}_0^{j-1} = \boldsymbol{\sigma}^{j-1}$, $\theta_0^{j-1} = \theta^{j-1}$ and $\boldsymbol{\gamma}_0^{j-1} = \boldsymbol{\gamma}^{j-1}$ as initial guesses. At the iteration i , $\boldsymbol{\sigma}_{i-1}^{j-1}, \boldsymbol{\gamma}_{i-1}^{j-1}, \theta_{i-1}^{j-1}$ are already computed and we look for $\mathbf{v}_i^{j-1}, \boldsymbol{\sigma}_i^{j-1}, \boldsymbol{\gamma}_i^{j-1}, \theta_i^{j-1}$.

First, we compute \mathbf{v}_i^{j-1} solving the following quadratic minimization problem

$$\mathbf{v}_i^{j-1} \in \mathcal{W}_h, \quad \mathcal{L}_k(\mathbf{v}_i^{j-1}, \boldsymbol{\sigma}_{i-1}^{j-1}, \theta_{i-1}^{j-1}, \boldsymbol{\gamma}_{i-1}^{j-1}) = \inf_{\mathbf{v} \in \mathcal{W}_h} \mathcal{L}_k(\mathbf{v}, \boldsymbol{\sigma}_{i-1}^{j-1}, \theta_{i-1}^{j-1}, \boldsymbol{\gamma}_{i-1}^{j-1}).$$

Then, we compute explicitly $\boldsymbol{\gamma}_i^{j-1}$ and θ_i^{j-1} through the functions f_H and \mathbf{f}_D

$$\boldsymbol{\gamma}_i^{j-1} = \mathbf{f}_D(\boldsymbol{\sigma}_{i-1}^{j-1} + 2r_D \mathbf{D}(\mathbf{v}_i^{j-1}), 2r_D), \quad \theta_i^{j-1} = f_H(\boldsymbol{\sigma}_{i-1}^{j-1} + 2r_H \mathbf{D}(\mathbf{v}_i^{j-1})), 2r_H)$$

and we update $\boldsymbol{\sigma}_i^{j-1}$ through the following formulas:

$$(\boldsymbol{\sigma}_i^{j-1})' = (\boldsymbol{\sigma}_{i-1}^{j-1})' + 2r_D (\mathbf{D}'(\mathbf{v}_i^{j-1}) - \boldsymbol{\gamma}_i^{j-1}),$$

$$\operatorname{trace}(\boldsymbol{\sigma}_i^{j-1}) = \operatorname{trace}(\boldsymbol{\sigma}_{i-1}^{j-1}) + 2r_H (\operatorname{div} \mathbf{v}_i^{j-1} - \theta_i^{j-1}).$$

The (UA) algorithm stops at $i = i_j^e$ when the error $e = \frac{\|\mathbf{v}_i^{j-1} - \mathbf{v}_{i-1}^{j-1}\|_{L^2(\mathcal{D}_0)}}{\|\mathbf{v}_i^{j-1}\|_{L^2(\mathcal{D}_0)}}$ is small enough. Then we update: $u^j = u_{i_j^e}^{j-1}, \boldsymbol{\sigma}^j = \boldsymbol{\sigma}_{i_j^e}^{j-1}, \theta^j = \theta_{i_j^e}^{j-1}$ and $\boldsymbol{\gamma}^j = \boldsymbol{\gamma}_{i_j^e}^{j-1}$. In

the numerical computations, when the solution \mathbf{v}^{j-2} is close to \mathbf{v}^{j-1} (for instance when Δt is small enough), a single pass of Uzawa-type algorithm (i.e. $i_k^e \equiv 1$) can be enough to satisfy the stop criterion in i . This fact reduces significantly the total computation time.

The algorithm (IA) stops at $j = j^e$, when the error $\frac{\|\mathbf{v}^j - \mathbf{v}^{j-1}\|_{L^2(\mathcal{D}_0)}}{\|\mathbf{v}^j\|_{L^2(\mathcal{D}_0)}}$ is small enough.

3.4.4 The density/damage problem

We will use a finite volume method (see for instance [29]) to discretize the continuity equation (82) and the damage evolution equation (86). Let denote by \mathcal{K}_h the finite volume mesh, which is given by a family of disjoint polygonal connected subsets of \mathbb{R}^3 such that $\overline{\mathcal{D}}$ is the union of the closure of the elements of \mathcal{K}_h ; h is the greatest diameter of a control volume in \mathcal{K}_h . The finite volume mesh \mathcal{K}_h may coincide (or not) with the finite element triangulation \mathcal{T}_h . In the simulations presented in the next section $\mathcal{K}_h \equiv \mathcal{T}_h$.

The finite volume discrete space is the space of piecewise constant functions, i.e. we are looking for the solution ρ_h of (82) and δ_h of (86) as $\{\rho_{hK}, K \in \mathcal{K}_h\}$ and $\{\delta_{hK}, K \in \mathcal{K}_h\}$, respectively. In order to simplify the notations, throughout this subsection we omit all the indexes h .

Let us consider two control volumes $K, P \in \mathcal{K}_h$ with a common interface $I_{KL} = \overline{K} \cap \overline{P}$. Let \mathbf{n} be the unit normal vector to I_{KP} oriented from K to P . Then, we define the flux $F(K, P)$ at the interface I_{KP} as

$$F(K, P) = \int_{I_{KP}} [\mathbf{v} \cdot \mathbf{n}]_+.$$

Note that at least one of the two fluxes $F(K, P)$ and $F(P, K)$ is vanishing. If we denote by $\mathcal{N}(K)$ the set of all neighbors of the control volume K , then the finite volume numerical scheme for (82) and (86) can be written as two linear algebraic systems for the unknowns $(\rho_K)_{K \in \mathcal{K}_h}$ and $(\delta_K)_{K \in \mathcal{K}_h}$

$$m(K)\rho_K + \Delta t \sum_{P \in \mathcal{N}(K)} F(K, P)\rho_K - F(P, K)\rho_P = m(K)\rho_K^k, \quad \text{for all } K \in \mathcal{K}_h. \quad (93)$$

$$m(K)\delta_K + \Delta t \sum_{P \in \mathcal{N}(K)} F(K, P)\delta_K - F(P, K)\delta_P = m(K)H^{k,n}, \quad \text{for all } K \in \mathcal{K}_h. \quad (94)$$

If a volume control L corresponds to a node which is on the boundary Γ_m , then we set $\rho_P = \rho_0, \delta_P = 0$ and we eliminate the corresponding equation.

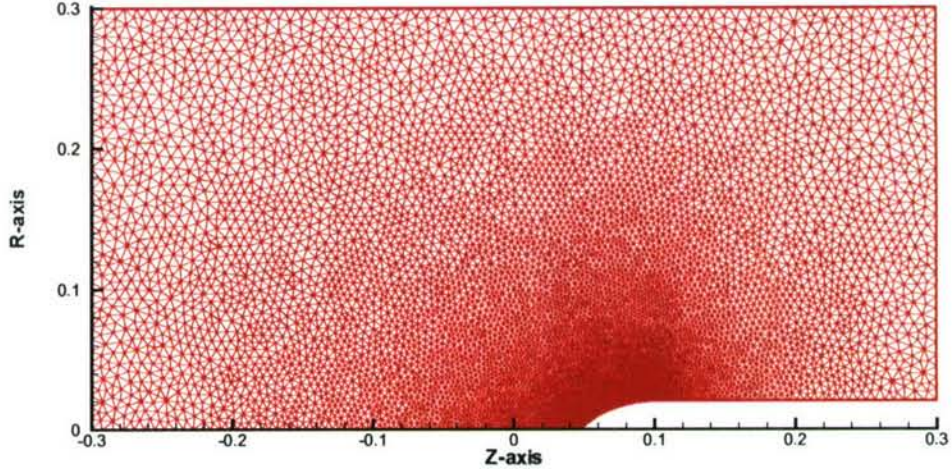


Figure 9: The finite element mesh.

3.5 Numerical results

In this section, we apply the material and computational model developed to simulate the tunneling phase of penetration into a concrete target of a rigid projectile. The simulations correspond to an impact velocity of $V_0 = 500$ m/s and a projectile of mass $M = 6$ kg.

3.5.1 Geometrical and physical settings

Preliminary numerical simulations, in which a part of the tunnel was considered in \mathcal{D}_0 have shown that the material behind the projectile is rigid and thus does not affect the computations. Hence, to reduce the computational efforts, the control volume \mathcal{D}_0 is chosen such that it does not touch the tunnel, i.e. $\Gamma_1 = \emptyset$.

The finite element mesh of the domain \mathcal{D}_0 in cylindrical coordinates (in the Orz plane), is plotted in Figure 9. It has 33169 nodes and 167666 triangular elements. The finite volume mesh may coincide with the finite element triangulation.

In a computation of the entire penetration process, the initial conditions for the tunnelling phase should correspond to the final state attained in the previous phase, called "sabot impact phase" (i.e. the phase when the projectile is fully embedded in the target and the pusher plate hits the target and strips off). However, in order to compute this state, it is necessary to model all the phases of penetration process (including the nose penetration phase and partially restrained penetration phase corresponding to chipping and cratering at the point of impact), which is beyond the scope of the present paper. Thus, in this work we consider that the

initial conditions $\mathbf{v}_0, \rho_0, \delta_0$ are given by the stationary solution corresponding to the striking velocity $V_0 = 500$ m/s. The solution of the stationary problem is computed using the techniques developed in our previous work [17].

The time interval for the computations, $[0, T]$, is chosen such that at $t = T$, the velocity of the projectile is $V(T) = V_{min} = 50$ m/s. This choice of V_{min} is related to the fact that for very low velocities (i.e. $V(t) < V_{min} = 50$ m/s) elastic effects, which were neglected in our model, become important with respect to the plastic ones. Note however that the phase of the process which is not modeled in this work (i.e. for $V(t) < V_{min} = 50$ m/s) corresponds to less than 5 % of the entire trajectory.

The specific expressions of the constitutive functions $\kappa(\mu, \delta)$ and $p_c(\mu)$, involved in the material model (equations (68)-(69)) are taken from Holmquist et al. [30]. The function p_c is expressed in terms of $\mu = \rho/\rho^0 - 1$ as:

$$\begin{cases} p_c(\mu) = \mu \frac{p_{crush}}{\mu_{crush}} & \text{if } \mu \leq \mu_{crush}, \\ p_c(\mu) = p_{crush} + \frac{(\mu - \mu_{crush})(p_{lock} - p_{crush})}{\mu_{lock} - \mu_{crush}} & \text{if } \mu \in [\mu_{crush}, \mu_*], \\ p_c(\mu) = K_1 \frac{\mu - \mu_{lock}}{1 + \mu_{lock}} + K_2 \left[\frac{\mu - \mu_{lock}}{1 + \mu_{lock}} \right]^2 + K_3 \left[\frac{\mu - \mu_{lock}}{1 + \mu_{lock}} \right]^3 & \text{if } \mu \geq \mu_*. \end{cases} \quad (95)$$

The values of the material constants involved in the above equation are: $p_{crush} = 16$ MPa, $p_{lock} = 800$ MPa, $\mu_{crush} = 0.001$, $\mu_{lock} = 0.1$, $\mu_* = 0.111$, $K_1 = 85$ GPa, $K_2 = -171$ GPa, and $K_3 = 208$ GPa (see [30]).

The yield limit in shear, $\kappa(\mu, \delta)$, which depends on both the compaction level and damage is expressed as

$$\kappa(\mu, \delta) = \sigma_0 \sqrt{2/3} \min\{S_{max}, A(1 - \delta) + B(p_c(\mu)/\sigma_0)^N\}. \quad (96)$$

with $\sigma_0 = 48$ MPa, $S_{max} = 7$, $A = 0.79$, $B = 1.60$, and $N = 0.61$. Following [30], it is assumed that the loss of cohesive strength of the concrete material is related to damage from irreversible deformation, which evolves according to the following law:

$$\frac{\partial \delta}{\partial t} + \mathbf{v} \cdot \nabla \delta = \frac{|\mathbf{D}'(\mathbf{v})|}{\Delta(\mu)}, \quad (97)$$

where $\Delta(\mu) = \sqrt{2/3} \max\{r_0, D_1[(p_c(\mu) + T)/\sigma_0]^{D_2}\}$, where r_0 , D_1 , D_2 are constants ($r_0 = 0.01$, $D_1 = 0.04$, $D_2 = 1$ for the given material) and T is the maximum tensile hydrostatic pressure that the material can withstand. For the concrete material studied, $T = 4$ MPa. Note that using the continuity equation and the definition of μ , we have:

$$\frac{\partial \mu}{\partial t} + \mathbf{v} \cdot \nabla \mu = -(1 + \mu) \operatorname{div}(\mathbf{v}),$$

Thus, the model for concrete is of the general form (66) with $n = 2$, $\mathbf{h} = (\mu, \delta)$ and

$$\mathbf{H}(\mathbf{D}(\mathbf{v}), \mathbf{h}) = (-(1 + \mu) \operatorname{div}(\mathbf{v}), |\mathbf{D}'(\mathbf{v})|/\Delta(\mu)).$$

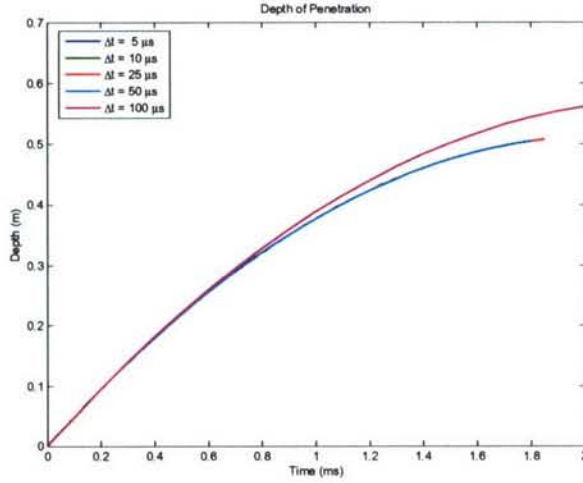


Figure 10: Penetration depth as a function of time for different time steps.

The volume and shear viscosity coefficients are considered constant and have the reference values $\lambda = 0.002 \text{ MPa}\cdot\text{s}$ and $\eta = 0.001 \text{ MPa}\cdot\text{s}$.

Frictional contact is assumed on the boundary Γ_2 of the projectile (see Figure 1). To account for rate effects on the frictional contact between the concrete target and the metallic penetrator, a decaying exponential dependence on the slip rate proposed in [31].

$$\mathcal{F}(v) = \mathcal{F}_\infty + \exp(-c_f v/v_0)(\mathcal{F}_0 - \mathcal{F}_\infty).$$

was considered. In the above equation, \mathcal{F}_0 represents the static value of the friction coefficient, while \mathcal{F}_∞ is its dynamic value, while c_f is a constant. Since experimental determination of the values of these coefficients is very difficult, the values of these coefficients were set to: $\mathcal{F}_\infty = 0.02$, $\mathcal{F}_0 = 0.2$, $v_0 = 1 \text{ m/s}$ and $c_f = 0.01$.

The boundary condition $u_n = 0$ prescribed on the projectile is accurate everywhere with the exception of two small zones. The first one is located on the nose of the projectile. In this zone, fracture in the target material could create a free boundary. A second zone, which is located on the shank of the projectile, corresponds to the separation between the target material and the projectile. The formulation and solution of these two free boundary problems is beyond the scope of this study. However, the influence of these two zones on the resistance to penetration seems to be very small.

3.5.2 Time step sensitivity

Let first check the time step sensitivity of the proposed explicit/implicit discretization scheme. To this end, simulations were performed using time steps Δt varying

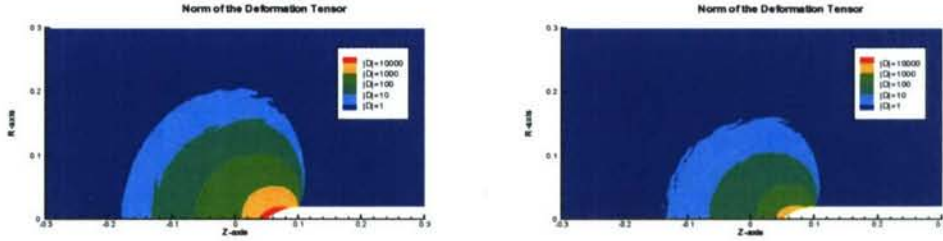


Figure 11: The distribution of the deformation rate $|\mathbf{D}(\mathbf{v})|$ (s^{-1}) in the target. Left: at the initial stage of the computations ($t = 0, V = 500m/s$). Right: at the final stage of the computations ($t = 1.85ms, V = 50m/s$).

from $5 \mu s$ to $100 \mu s$. Figure 10 shows the evolution of the penetration depth D_p :

$$D_p(t) =: \int_0^t V(s), ds$$

versus time for different time steps Δt . It is clear that even for a coarse time step $\Delta t = 50\mu s$, which corresponds to only 36 time iterations, the penetration depth is accurately predicted. However, for time steps Δt larger than $100\mu s$ the time discretization error can be important. We conclude that the time discretization scheme is robust and, since we can use a small number of time iterations, the computational cost is low.

3.5.3 Fields distribution in the target

In Figure 11 is shown the distribution of the deformation rate $|\mathbf{D}(\mathbf{v})|$ in the target corresponding to the initial and final stages of the computations, respectively for an impact velocity of 500 m/s. It is seen that a viscoplastic zone develops around the penetrator. Outside this zone there is no deformation, hence the target is rigid, i.e. $|\mathbf{D}(\mathbf{v})|$ vanishes. It can be observed that the maximum deformation rate is reached on the nose tip. The visco-plastic zone is diminishing during the penetration process.

Figure 12 (left) shows the distribution of density in the target at $t = 0.925ms$, an intermediate time in the computation. Note the existence of three distinct zones: (1) an (almost) incompressible zone around the penetrator where the concrete is almost fully compacted ($\mu > \mu_*$) ; (2) a compressible zone where the density is greater than ρ_0 , the density of the intact material, and (3) a zone that remains unaffected by the impact event where the density is everywhere equal to ρ_0 . It is worth noting that all the particles ahead of the projectile which are at a distance from the centerline less than the projectile radius will enter the fully compacted zone (1).

In Figure 12 (right) is depicted the distribution of damage (parameter δ) in the target at an intermediate time of the computation: $t = 0.925ms$. Fully damaged state corresponds to $\delta = 1$ while $\delta = 0$ corresponds to no-damage. Let note that

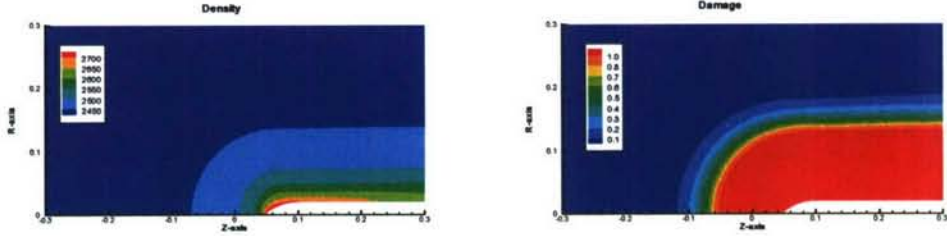


Figure 12: Left: the distribution of the density ρ (kg/m^3) in the target at $t = 0.925ms$. Right: the distribution of damage δ in the target at $t = 0.925ms$.

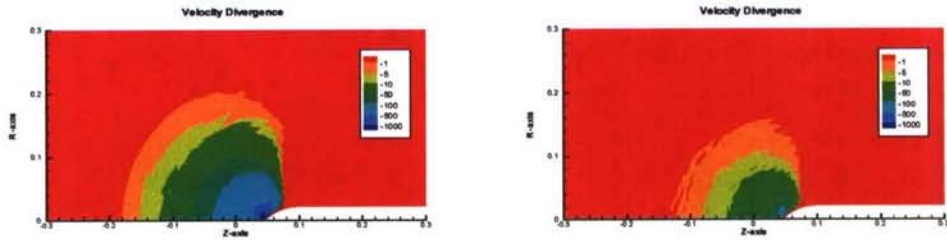


Figure 13: The distribution of the rate of volumetric deformation $\text{div } \mathbf{v}$ (s^{-1}) in the target. Left: at the initial stage of the computations ($t = 0, V = 500m/s$). Right: at the final stage of the computations ($t = 1.85ms, V = 50m/s$).

according to the model, a large zone of the target is fully damaged. The extent of the fully damaged zone varies little during the penetration process (i.e. there is little variation with $V(t)$).

The distribution of the rate of volumetric deformation $\text{div } \mathbf{v}$ at the initial and final stages of the computations are plotted in Figure 13. We note that around the penetrator an almost fully compacted state is achieved, the material being almost incompressible. The maximum compaction is reached in the nose zone, ahead of the projectile.

Let us analyze now the stress distribution in the target and determine the zones where tensile failure may occur. It is assumed that concrete tensile failure can be modeled with the classic maximum tensile strength criterion (see [32]), i.e. the material fails if the maximum of the principal stresses reaches a critical limit denoted σ_f . From the data reported in [30] $\sigma_f = 4$ MPa. From the analysis of the stress distribution in the target, we found that the only principal stress which can have positive values (i.e. is tensile) is $\sigma_{\theta\theta}$ (see regions in green in figure 14). As shown in figure 14 tensile failure occurs in a wide region (colored in red) ahead of the projectile. This region is smaller for low projectile velocities i.e. at the end of the penetration process. From this analysis, fundamental understanding of the stability

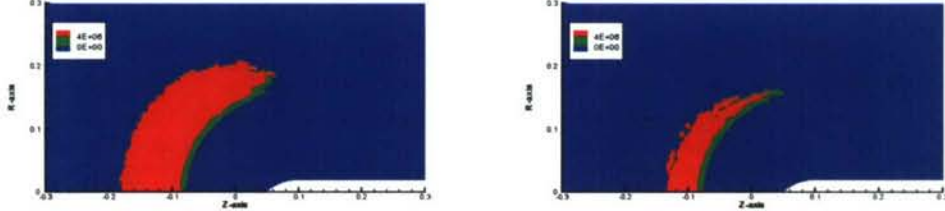


Figure 14: The distribution of $\sigma_{\theta\theta}$ in the target. In green the region which are in tensile ($\sigma_{\theta\theta} \geq 0$) and in red the regions where tensile failure occurs ($\sigma_{\theta\theta} \geq \sigma_f$). Left: at the initial stage ($t = 0, V = 500\text{m/s}$). Right: at the final stage of the computations ($t = 1.85\text{ms}, V = 50\text{m/s}$).

of the penetrator trajectory can be gained. Indeed, since the tensile failure could occur only along Ozr planes, orthogonal to \mathbf{e}_θ , which are not symmetric with respect to the penetrator centerline, anisotropy is generated in the target. Trajectory deviations, observed at high penetration velocities, may be related to this induced anisotropy.

3.5.4 Parameter sensitivity of the penetration depth

As already mentioned, one of the many challenges associated with modeling penetration is that only very limited experimental information such as projectile trajectory and deceleration data can be gathered during penetration. To date, there is limited data from which the yield strengths may be inferred and thus the cut-off yield limit S_{max} involved in the expression (96) of the shear yield limit κ cannot be determined explicitly. Likewise, it is very difficult to evaluate experimentally the viscous coefficients λ and η , and the coefficient c_f , involved in the friction law. Because of the lack of test data, a parametric study was conducted to estimate the sensitivity of the depth of penetration predictions to these constants.

First it was assessed the importance of plastic versus viscous effects on the penetration depth. To better analyze these effects, friction was completely neglected, i.e. we set $\mathcal{F} \equiv 0$.

To estimate the influence of viscosity on the penetration depth, we have set all the parameters involved in the expression of κ , the yield limit in shear, and of p_c to be equal to the reference values and we have performed a series of numerical simulations in which we varied the values of the viscous parameters η and λ . In Figure 15 are plotted the evolution of the penetration depth $t \rightarrow D_p(t)$ with time for different values of the shear viscosities η . In all these calculations, the volume viscosity λ was held constant (i.e. equal to the reference value). It is clearly seen that for η less than 1000 Pa·s, the plastic properties of the target are dominant while the viscous effects are negligible.

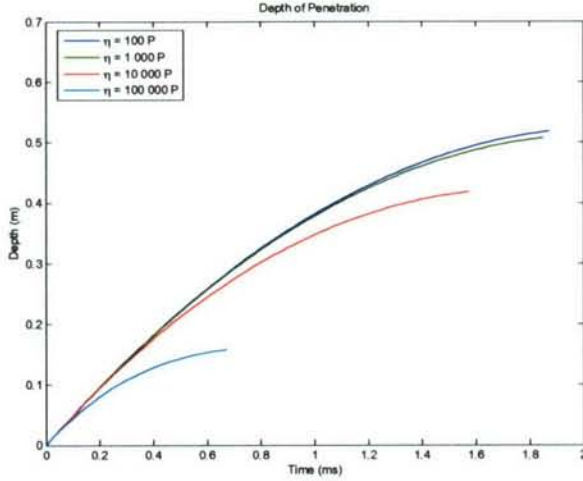


Figure 15: Evolution of penetration depth $t \rightarrow D_p(t)$ for different shear viscosities η .

However, for η greater than 1000 Pa·s, the viscous effects are more pronounced. Indeed, in the range of $10^3 - 10^5$ Pa·s a variation of two orders of magnitude of the value of η gives rise to an order of magnitude variation in penetration depth.

We have also computed the evolution of the penetration depth $t \rightarrow D_p(t)$ for different values of the volume viscosity λ in the range of $10^2 - 10^5$ Pa·s. In all the calculations, the shear viscosity η was held constant (equal to a reference value). We have found that the volume viscosity has no influence on the penetration depth. An explanation of this insensitivity to the volume viscosity could be the fact that around the projectile the target material is almost incompressible (see figures 12 and 13), hence the volume strain rate $\text{div}(\mathbf{v})$ is very small. That means that the stress distribution around the projectile is not affected by the volume viscosity λ which multiplies $\text{div}(\mathbf{v})$. Since the resistance force, involved in the calculation of the penetration depth, is computed based only on the distribution of the stress tensor $\boldsymbol{\sigma}$ on the projectile surface, we can deduce that one cannot expect any variation of the resistance force with respect to the volumetric viscosity λ .

In addition, since it is very difficult to determine experimentally the viscosity coefficients of concrete for dynamic loading (high rate of deformations and high stresses), the sensitivity analysis performed is important in selecting the numerical values of these constants that will provide the best fit to the penetration depths which are directly measured in penetration tests.

In order to see the effects of the plastic parameters, we set the the viscous parameters λ and η equal to the reference values and we performed a series of numerical simulations for different values of the cut-off yield limit S_{max} , parameter involved in the expression of the yield limit κ which cannot be obtained from experiments in

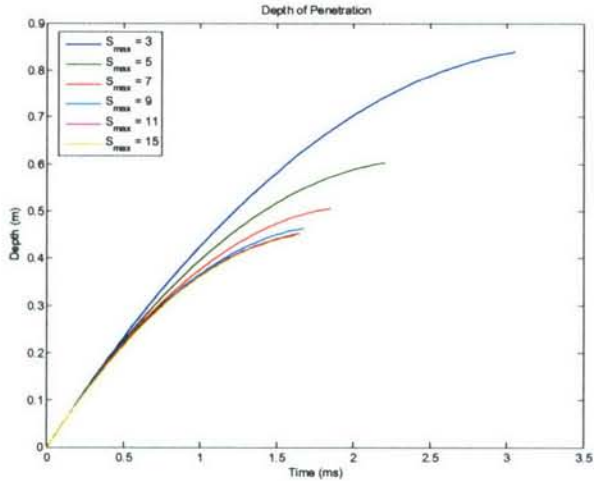


Figure 16: Evolution of penetration depth $t \rightarrow D_p(t)$ for different values of the cut-off yield limit S_{max} .

an explicit manner. As in the previous calculations, we have completely neglected friction i.e. we took ($\mathcal{F} \equiv 0$).

In Figure 16 is plotted the evolution of the penetration depth $t \rightarrow D_p(t)$ for different values of the cut-off yield limit S_{max} . Note that for S_{max} greater than 9, there is little influence on the penetration depth. That means that near to the projectile, the pressures $B(p_c(\mu)/\sigma_0)^N$ are less than the cut-off value S_{max} . If S_{max} is less than 9, then S_{max} constitutes a limit on the strength that can be developed in the material (i.e. really works as a cut-off value for the yield strength). In this case, it was found that the penetration depth is very sensitive to the yield stress. Indeed, if S_{max} is three times smaller then the final penetration depth is three times larger.

Next, the effect on the penetration depth of the coefficient c_f , involved in the slip rate weakening friction law was analyzed. To this end, we held all the other parameters constant (i.e. we set \mathcal{F}_0 and \mathcal{F}_∞ and all the coefficients involved in the model for the target equal to reference values). In Figure 17 is plotted the evolution of penetration depth $t \rightarrow D_p(t)$ for different values of c_f . We note that if c_f is greater than 0.01 it doesn't have any effect on the final penetration depth. In this case, the friction coefficient reaches its dynamical value \mathcal{F}_∞ almost at every point on the projectile. If c_f is less than 0.01, then the slip rate weakening of the friction coefficient becomes apparent, i.e. the penetration depth is also sensitive to the value of the static friction coefficient \mathcal{F}_0 .

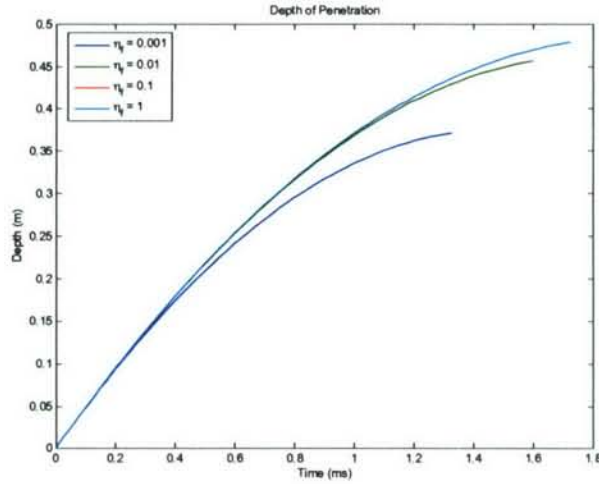


Figure 17: Evolution of penetration depth $t \rightarrow D_p(t)$ for different values of the exponential decrease coefficient c_f , involved in the slip rate weakening friction law.

4 Conclusions

We have developed computational methods for modeling the penetration of a rigid projectile into porous geological and cementitious targets. To capture the solid-fluid transition in behavior at high strain rates observed in such media and account for damage/plasticity couplings and how these dissipative mechanisms are influenced by the strain rate, a compressible rigid viscoplastic fluid constitutive equation was considered. A hybrid time-discretization was used to model the non-stationary flow of the target, i.e. an explicit Euler method for the projectile equation and a forward (implicit) method for the target boundary value problem. At each time step, a mixed finite-element and finite-volume strategy was used to solve the "target" boundary value problem.

Specifically, variational formulations and algorithms for solving the minimization problems with non-linear constraints for the velocity field via the finite element approximation were developed while finite-volume techniques were adopted for solving the hyperbolic mass conservation and damage evolution equations. Since in the constitutive description of the target material a rigid unloading hypothesis was considered, the variational inequality to be solved has unilateral constraints for the velocity divergence. Additional difficulties were related to ensuring incompressibility in the regions where the material is unloading. Also, due to plastic and frictional contributions, the resulting functional is not smooth. To overcome these difficulties, the decomposition-coordination formulation coupled with the augmented lagrangian method proposed for the incompressible Bingham fluid by [19, 20] was adapted for the material model considered in this work.

Numerical simulations of penetration into concrete were performed. It was shown that using the model and numerical techniques presented in this paper, it is possible to predict the density changes around the penetration tunnel, the shape and location of the rigid/plastic boundary, the extent of damage due to air void collapse in such materials. According to our calculations, tensile failure occurs ahead of the penetrator and along planes which are not symmetric with respect to the penetrator centerline. This induced anisotropy may explain trajectory deviations.

One of the many challenges associated with simulating penetration in cementitious materials is related to the lack of experimental data for the high pressures and high strain rates involved. Thus, some of the constants involved in the model cannot be determined directly from experimental data. A parametric study was performed to assess the sensitivity of the predicted penetration depth to these constants (i.e. to shear and volumetric viscosities, cut-off yield limit, and dynamic friction coefficients). The results of this parametric study provides insights into the relative importance of the plastic and viscous effects on the penetration process. Finally, by conducting a time step sensitivity study it was shown that the numerical model is robust and computationally inexpensive.

References

- [1] Gran, J.K. and Frew, D.J. (1997), In-target radial stress measurements from penetration experiments into concrete by ogive-nose steel projectiles, *Int. J. Impact Engng.* 715-726.
- [2] Hertel, E. S. (1997), A survey of numerical methods for shock physics applications, *International Workshop on New Models and Numerical Codes for Shock Wave Processes in Condensed Media*, September 15-19, 1997, Oxford, England.
- [3] Duarte, A. and Oden, J. T. (1997), An h-p adaptive method using clouds, *Comput. Methods Appl. Mech. Engrg.* 142:269-301.
- [4] Johnson, G. R., Stryk, R. A. and Beissel, S. R. (1996), SPH for high velocity impact computations, *Comput. Methods Appl. Mech. Engrg.* 139: 237-262.
- [5] Liu, W.-K, Hao, S., Belytschko, T., Li, S. and Chang, C.T. (2000), Multi-scale methods, *Int. J. Numer. Methods Engrg.*, 47 (7).
- [6] Belytschko, T., Guo, Y., Liu, W.-K. and Xiao, S.P. (2000), Unified stability analysis of meshless particle methods, *Int. J. Numer. Methods Engrg.*, 48 (9).
- [7] Dolbow, J., Moes, N. and Belytschko, T. (2000), Discontinuous enrichment in finite element with a partition of unity method, *Finite Elements Anal. Des.* 36 (3).

- [8] J. Donea, A. Huerta, J. Ph. Ponthot and A. Rodirguez-Ferran (2004), Arbitrary Lagrangian-Eulerian Methods, *Encyclopedia of Computational Mechanics*, E. Stein, R. de Borst and T.J.R. Hugues editors, John Wiley & Sons
- [9] R. C. Batra (1987), Steady-state penetration of viscoplastic targets, *Int. J. Engng. Sci.*, 25, pp. 1131–1141.
- [10] R. C. Batra and A. Adam (1991), Effect of viscoplastic flow rules on steady state penetration of thermoviscoplastic targets, *Int. J. Engng. Sci.* 29, 1391–1408.
- [11] Frew, D.J., Forrestal, M.J. , Cargile, J.D.(2006), The effect of concrete target diameter on projectile deceleration and penetration depth, *Int. J. Impact Eng.*, in press
- [12] J.A. Zukas, T. Nicholas, H. F. Swift, L.B. Greszczuk and D. R. Curran (1992), Penetration and perforation of solids, *Impact Dynamics*, Krieger Publishing Company, Malabor, FL, 155–214.
- [13] Heuze, F. E. (1990), An overview of projectile penetration into geologic materials, with emphasis on rocks. *Int. J. Rock Mech. Min. Sci.*, 27, 1–14.
- [14] R. C. Batra and T. Gobinath (1988), Steady-state penetration of compressible perfectly plastic targets, *Int. J. Engng. Sci.*, 26, 741–751.
- [15] Gao Shi-qiao, Liu Hai-peng, Li Ke-jie, Huang Feng-lei and Jin Lei, (2006), Normal expansion theory for penetration of projectile against concrete target, *Applied Mathematics and Mechanics*, 27, No. 4, 485-492.
- [16] Yuh-Shiou Tai and Chia-Chih Tang, (2006), Numerical simulation: The dynamic behavior of reinforced concrete plates under normal impact, *Theoretical and Applied Fracture Mechanics*, 45, Issue 2, Pages 117–127.
- [17] O. Cazacu, I. R. Ionescu and T. Perrot (2006), Steady-state flow of compressible rigid-viscoplastic media, *Int. J. Engng. Sci.*, vol 44, 1082–1097
- [18] O. Cazacu and I.R. Ionescu (2006), Compressible rigid visco-plastic fluids, *J. of Mech. Phys. of Solids*, Vol. 54, issue 8, 1640–1667.
- [19] M. Fortin and R. Glowinski (1982), *Méthodes de Lagrangien augmentés, application à la résolution de problèmes aux limites*, Dunod.
- [20] R. Glowinski and P. Le Tallec (1989), *Augmented Lagrangian and Operator Splitting method in Non-Linear Mechanics*, SIAM Studies in Applied Mathematics

[21] E.J. Dean, R. Glowinski and G. Guidoboni (2007), On the numerical simulation of Bingham visco-plastic flow: old and new results, *J. Non-Newtonian Fluid Mech.*, 142, 36-62

[22] Gebbeken, N., Greulich, S., Pietzsch, A. (2006), Hugoniot properties for concrete determined by full-scale detonation experiments and flyer-plate-impact tests, *Int. J. Impact Engng.*, 32, 2017–2031.

[23] E. Wiliams, S.A. Akers and P.A. Reed (2005), Laboratory characterization of fine aggregate cementitious material, *Geotechnical and Structures Laboratory*, ERDC/GLS TR-05-16,

[24] S. J. Jones, D.M.Jerome, L. Wilson, and F.R. Christophe (1998), An engineering analysis of normal rigid body penetration into concrete, *Structures Under Extreme Loading Conditions, ASME, PVP-Vol 361*, 63–67.

[25] O. Pironneau, (1989), *Finite element methods for fluids*, John Wiley & Sons Ltd., Chichester.

[26] R. Temam (1979), *Navier-Stokes Equations. Theory and Numerical Analysis*, North-Holland, Amsterdam.

[27] I. R. Ionescu and M. Sofonea (1993), *Functional and numerical methods in viscoplasticity.*, Oxford University Press.

[28] I. Ionescu and B. Vernescu (1988), A numerical method for a viscoplastic problem. An application to the wire drawing, *Int. J. Engng. Sci.*, 26 , 627–633.

[29] R. Eymard, T. Gallouet, R. Herbin (2000), The finite volume method, *Handbook for Numerical Analysis*, Ph. Ciarlet J.L. Lions eds, North Holland, 715–1022.

[30] Holmquist, T.J. , Johnson, G.R., Cook, W.H., (1993), A computational constitutive model for concrete subjected to large strains, high strain rates, and high pressures, *14th Int. Symp. on Ballistics*, Quebec-City, Canada.

[31] E.P. Chen, E.D. Reedy, (1991), Penetration into Geological Targets: Numerical Studies on Sliding Friction, in *Computational Aspects of Contact, Impact and Penetration*, R.K. Kulak Ed., Elmepress International

[32] W. Rankine (1972), *Applied Mechanics*, Charles Griffin and Company, London